THE JOURNAL OF PHYSICAL CHEMISTRY A
A JOURNAL OF THE AMERICAN CHEMICAL SOCIETY

pubs.acs.org/JPCA
Article

Acetonyl Peroxy and Hydroperoxy Self- and Cross-Reactions: Temperature-Dependent Kinetic Parameters, Branching Fractions, and Chaperone Effects

Published as part of The Journal of Physical Chemistry virtual special issue "Marsha I. Lester Festschrift".

Kristen Zuraski, Fred J. Grieman, Aileen O. Hui, Julia Cowen, Frank A. F. Winiberg, Carl J. Percival, Mitchio Okumura, and Stanley P. Sander*

Cite This: *J. Phys. Chem. A* 2023, 127, 7772−7792

ABSTRACT: The temperature-dependent kinetic parameters, branching fractions, and chaperone effects of the self- and cross-reactions between acetonyl peroxy ($CH_3C(O)CH_2O_2$) and hydro peroxy (HO_2) have been studied using pulsed laser photolysis coupled with infrared (IR) wavelength-modulation spectroscopy and ultraviolet absorption (UVA) spectroscopy. Two IR lasers simultaneously monitored HO_2 and hydroxyl (OH), while UVA measurements monitored $CH_3C(O)CH_2O_2$. For the $CH_3C(O)CH_2O_2$ self-reaction (T = 270−330 K), the rate parameters were determined to be $A = (1.5^{+0.4}_{-0.3}) \times 10^{-13}$ and $E_a/R = -996 \pm 334$ K and the branching fraction to the alkoxy channel, k_{2b}/k_2, showed an inverse temperature dependence following the expression, $k_{2b}/k_2 = (2.27 \pm 0.62) - [(6.35 \pm 2.06) \times 10^{-3}]\ T(\mathrm{K})$. For the reaction between $CH_3C(O)CH_2O_2$ and HO_2 (T = 270−330 K), the rate parameters were determined to be $A = (3.4^{+2.5}_{-1.5}) \times 10^{-13}$ and $E_a/R = -547 \pm 415$ K for the hydroperoxide product channel and $A = (6.23^{+15.3}_{-4.4}) \times 10^{-17}$ and $E_a/R = -3100 \pm 870$ K for the OH product channel. The branching fraction for the OH channel, k_{1b}/k_1, follows the temperature-dependent expression, $k_{1b}/k_1 = (3.27 \pm 0.51) - [(9.6 \pm 1.7) \times 10^{-3}]\ T(\mathrm{K})$. Determination of these parameters required an extensive reaction kinetics model which included a re-evaluation of the temperature dependence of the HO_2 self-reaction chaperone enhancement parameters due to the methanol−hydroperoxy complex. The second-law thermodynamic parameters for $K_{P,M}$ for the formation of the complex were found to be $\Delta_r H^\circ_{250K} = -38.6 \pm 3.3$ kJ mol^{-1} and $\Delta_r S^\circ_{250K} = -110.5 \pm 13.2$ J mol^{-1} K^{-1}, with the third-law analysis yielding $\Delta_r H^\circ_{250K} = -37.5 \pm 0.25$ kJ mol^{-1}. The HO_2 self-reaction rate coefficient was determined to be $k_4 = (3.34^{+1.04}_{-0.80}) \times 10^{-13} \exp[(507 \pm 76)/T]$cm^3 molecule^{-1} s^{-1} with the enhancement term $k''_{4,M} = (2.7^{+4.7}_{-1.7}) \times 10^{-36} \exp[(4700 \pm 255)/T]$cm^6 molecule^{-2} s^{-1}, proportional to [CH_3OH], over T = 220−280 K. The equivalent chaperone enhancement parameter for the acetone-hydroperoxy complex was also required and determined to be $k''_{4,A} = (5.0 \times 10^{-38} - 1.4 \times 10^{-41}) \exp[(7396 \pm 1172)/T]$ cm^6 molecule^{-2} s^{-1}, proportional to [$CH_3C(O)CH_3$], over T = 270−296 K. From these parameters, the rate coefficients for the reactions between HO_2 and the respective complexes over the given temperature ranges can be estimated: for $HO_2{\cdot}CH_3OH$, $k_{12} = [(1.72 \pm 0.050) \times 10^{-11}] \exp[(314 \pm 7.2)/T]$ cm^3 molecule^{-1} s^{-1} and for $HO_2{\cdot}CH_3C(O)CH_3$, $k_{15} = [(7.9 \pm 0.72) \times 10^{-17}] \exp[(3881 \pm 25)/T]$ cm^3 molecule^{-1} s^{-1}. Lastly, an estimate of the rate coefficient for the $HO_2{\cdot}CH_3OH$ self-reaction was also determined to be $k_{13} = (1.3 \pm 0.45) \times 10^{-10}$ cm^3 molecule^{-1} s^{-1}.

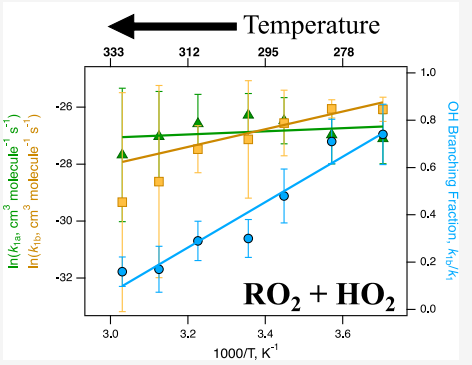

1. INTRODUCTION

Atmospheric composition in the troposphere is largely influenced by photochemically generated radical species. These radicals undergo reactions with volatile organic compounds (VOCs) to generate alkyl radicals that, through an oxygen (O_2) addition reaction, form metastable peroxy radicals, RO_2. Photolysis of carbonyl-containing VOCs, alkene ozonolysis, and radical recycling reactions also generate hydroperoxy radicals (HO_2) in the troposphere. In low-NO_x ($NO + NO_2$) environments, radical loss reactions between HO_2 and RO_2 play a vital role in dictating the HO_x (HO_2 and OH) and ozone budgets and, consequently, the oxidizing capacity of the troposphere, the Earth's radiative balance, and future changes in climate.[1−13]

Acetone ($CH_3C(O)CH_3$) is one of the most abundant oxygenated VOCs emitted into the atmosphere in pristine

Received: May 31, 2023
Revised: August 1, 2023
Published: September 8, 2023

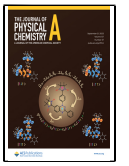

https://doi.org/10.1021/acs.jpca.3c03660
J. Phys. Chem. A 2023, 127, 7772−7792

environments and leads to the formation of the RO_2: acetonyl peroxy ($CH_3C(O)CH_2O_2$).[14−17] The cross-reactions between $CH_3C(O)CH_2O_2$ and HO_2, R1, as well as the $CH_3C(O)CH_2O_2$ self-reaction, R2, have been studied at room temperature.[18−27] R1 serves as either a temporary reservoir reaction in the atmosphere through the formation of hydroperoxides (ROOH, R1a) or as a radical propagation pathway by generating hydroxyl radicals (OH, R1b). For R2, there are three available pathways: R2a generates hydroxyacetone ($CH_3C(O)CH_2OH$) and methylglyoxal ($CH_3C(O)CHO$) as stable products, R2b generates the acetoxy radical ($CH_3C(O)CH_2O$), and R2c generates the higher functionalized accretion product (ROOR, $C_6H_{10}O_4$).[18,26]

$$CH_3C(O)CH_2O_2 + HO_2 \rightarrow CH_3C(O)CH_2OOH + O_2 \quad (R1a)$$

$$\rightarrow CH_3C(O)CH_2O + OH + O_2 \quad (R1b)$$

$$2CH_3C(O)CH_2O_2 \rightarrow CH_3C(O)CH_2OH + CH_3C(O)CHO + O_2 \quad (R2a)$$

$$\rightarrow 2CH_3C(O)CH_2O + O_2 \quad (R2b)$$

$$\rightarrow C_6H_{10}O_4(ROOR) + O_2 \quad (R2c)$$

Determining the branching fraction R1b/R1 is motivated by the need to accurately account for OH production pathways in atmospheric models to resolve discrepancies with OH field measurements.[29−32] Previous temperature dependence studies of other $RO_2 + HO_2$ reactions were shown to have reaction rate coefficients and branching fractions for OH production that are inversely dependent on temperature.[33] R2 is an additional loss pathway for RO_2 radicals. It is less dominant in the remote atmosphere compared to R1 due to the higher atmospheric concentrations of HO_2 relative to RO_2;[1,2] however, determining the kinetics and branching fractions for R2 is important for laboratory studies.

While studying R1 and R2 in a laboratory setting, the precursors, methanol (CH_3OH) and $CH_3C(O)CH_3$, used to generate the starting HO_2 and $CH_3C(O)CH_2O_2$ radicals, respectively, form the following reactive hydrogen-bonded (H-bonded) adducts with HO_2: $HO_2{\cdot}CH_3OH$ and $HO_2{\cdot}CH_3C(O)CH_3$.[18,34−38] In general, the formation of the radical adduct of HO_2 with some molecule, X, is described by the rapid equilibrium reaction

$$HO_2 + X \rightleftharpoons HO_2{\cdot}X \quad (R3)$$

These H-bonded adducts impact the observed overall kinetics of HO_2 reactions by accelerating the effective HO_2 self-reaction, R4, via a chaperone mechanism, R5a and R5b, which increases in rate as the temperature is lowered. Therefore, this effect needs to be quantitatively considered in our overall kinetics analysis which includes R4.

$$HO_2 + HO_2 \rightarrow H_2O_2 + O_2 \quad (R4)$$

$$HO_2 + HO_2{\cdot}X \rightarrow H_2O_2 + O_2 + X \quad (R5a)$$

$$HO_2{\cdot}X + HO_2{\cdot}X \rightarrow H_2O_2 + O_2 + 2X \quad (R5b)$$

R4 is an important sink for HO_x in the clean troposphere and is also the dominant source of stratospheric hydrogen peroxide, H_2O_2, which acts as a temporary reservoir for HO_x. The overall rate coefficient of R4, k_4, is pressure-dependent and is expressed as a sum of two terms

$$k_4 = k_{4,bi} + k_{4,ter}[M] \quad (E1)$$

where $k_{4,bi}$ is the pressure-independent bimolecular rate coefficient and $k_{4,ter}$ is the pressure-dependent termolecular rate coefficient. Christensen et al.[34] demonstrated that under high pressure and low radical concentrations, the equilibrium reaction of R3 for X = CH_3OH is established rapidly on a microsecond timescale as opposed to the millisecond timescale of the HO_2 loss rate through R1 and R4. Their work revealed that HO_2 loss followed second-order kinetic behavior, even with rate enhancement caused by the H-bonded adduct with CH_3OH. As a result, any unaccounted loss of HO_2 via R4 introduces systematic errors that propagate into errors in the determination of the rate coefficients of HO_2 reactions when CH_3OH is used as a radical precursor. Similarly, when $CH_3C(O)CH_3$ is present, the possible self-reaction rate enhancement caused by the analogous H-bonded adduct formed with $CH_3C(O)CH_3$ needs to be considered. Since equilibrium concentrations of these adducts increase as temperature decreases, the rate enhancement effect also has a temperature dependence that needs to be included in temperature-dependence laboratory studies of HO_2 reacting with peroxy radicals using these precursors.

In order to reconcile discrepancies in the current literature and to analyze the data measurements for our temperature dependence study of R1a and R2a, the equilibrium constants for the $HO_2{\cdot}CH_3OH$ and $HO_2{\cdot}CH_3C(O)CH_3$ formation reactions and the temperature dependence of the observed kinetic rate coefficients for R4 (which includes the enhancement caused by R5a) as a function of CH_3OH and $CH_3C(O)CH_3$ concentrations were investigated over the temperature range T = 220−296 K and T = 270−298 K, respectively. A reinvestigation of the thermodynamic parameters of the equilibrium reaction with CH_3OH was accomplished using a van't Hoff analysis over a wider temperature range than previously studied.[34] Analogous parameters for the $CH_3C(O)CH_3$ adduct were obtained in a previous study by Grieman et al.[38] Using these results, this work extends the previous room-temperature determination of the R1 and R2 reaction rate coefficients and branching fractions[18] to the temperature range, T = 270−330 K, and is reported here for the first time. In all experiments, the kinetics of the key reactants and products species were monitored using the infrared (IR) kinetics spectroscopy (IRKS) instrument which employs simultaneous time-resolved near-IR (NIR), mid-IR (MIR), and ultraviolet absorption spectroscopic (UVA) detection of HO_2, OH, and $CH_3C(O)CH_2O_2$, respectively.

2. METHODS

2.1. IRKS Instrument. The IRKS instrument and the chemical mechanism used for fitting the data to determine the temperature dependence for the rates, branching fractions, and chaperone effects of the self- and cross-reactions of $CH_3C(O)CH_2O_2$ and HO_2 have been described in the recent room-temperature kinetics publication[17] as well as in previous works.[31−33] The methodologies are described in brief here with an emphasis on details that pertain to this work. All experiments were initiated inside a temperature-controlled (T = 220−330 K, 2σ = 1 K) flow cell (175 cm long, 5 cm diameter). The temperature was controlled by flowing a silicone-based fluid (Syltherm) through the cell jacket from a chiller capable of both cooling and heating (Thermo Neslab ULT-95). In all experiments, the temperature was monitored with a calibrated type-T thermocouple (Omega), which was

https://doi.org/10.1021/acs.jpca.3c03660
J. Phys. Chem. A 2023, 127, 7772−7792

inserted into the jacket and was in contact with the temperature-controlling fluid.

2.2. Radical Generation. Pulsed laser photolysis by a XeF excimer laser (Lambda Physik Compex 301, 351 nm, 110 mJ/pulse in constant energy mode, 0.2 Hz repetition rate) was used to generate the starting radical, Cl, from Cl_2 (air products, 9.99% in He, $[Cl_2] = (0.8-10) \times 10^{15}$ molecule cm^{-3}). The range of total starting radical concentrations, $[Cl]_0$, following photolysis was $(0.2-2.2) \times 10^{14}$ molecule cm^{-3}. Depending on the experiment, nitrogen carrier gas was bubbled through CH_3OH (Fisher Optima A454-1, >99.9%, bubbler temperature = 0 °C) and/or $CH_3C(O)CH_3$ (Fisher Optima A929-1, >99.9%, bubbler temperature = −25 °C) to entrain these reagent species in the gas phase. Concentrations ranging from $[CH_3C(O)CH_3] = 1.7-2.8 \times 10^{16}$ and $[CH_3OH] = (1.0-25) \times 10^{15}$ molecule cm^{-3} were determined manometrically based on the measured pressures (absolute capacitance manometers, MKS Baratron) and regulated flow rates (mass flow controllers, MKS Instruments). Within the continuous flow cell, R6−R9 resulted in the generation of HO_2, $CH_3C(O)CH_2O_2$, or HO_2 + $CH_3C(O)CH_2O_2$, showing the self-reactions and cross-reactions, respectively.

$$Cl + CH_3OH \rightarrow CH_2OH + HCl \quad (R6)$$

$$CH_2OH + O_2 \rightarrow HO_2 + CH_2O \quad (R7)$$

$$Cl + CH_3C(O)CH_3 \rightarrow CH_3C(O)CH_2 + HCl \quad (R8)$$

$$CH_3C(O)CH_2 + O_2 \rightarrow CH_3C(O)CH_2O_2 \quad (R9)$$

The gas-phase Cl_2, CH_3OH, and $CH_3(O)CH_3$ were premixed with O_2 (Airgas Corps., 99.996%, $[O_2] = 1.6 \times 10^{18}$ molecule cm^{-3}) and N_2 bath gas (Airgas Corps., 99.997%) in a jacketed Pyrex manifold and thermally equilibrated to the selected reaction temperature prior to being introduced to the flow cell. The flow cell pressure was held constant at 100 Torr, the total flow rate was set to 2160 sccm, and the flow cell residence time was 9.7 s. For experiments focusing on the cross-reaction, secondary chemistry from the $CH_3C(O)CH_2O_2$ self-reaction was minimized by keeping $[HO_2]$ in excess of $[CH_3C(O)CH_2O_2]$ using ratios of $[HO_2]/[CH_3C(O)CH_2O_2] = 4-6$.

2.3. Detection of $CH_3C(O)CH_2O_2$, HO_2, and OH. UVA and IR-wavelength modulation spectroscopy (WMS) techniques were used to monitor the time-dependent concentrations of $CH_3C(O)CH_2O_2$, HO_2, and the product OH radicals. $CH_3C(O)CH_2O_2$ concentrations were monitored using 312 nm UV light, where $CH_3C(O)CH_2O_2$ has spectral absorption distinct from all of the other radical species present in the reactions studied.[18] Two independent continuous-wave distributed feedback IR lasers (NASA JPL Microdevices Laboratory) monitored the concentrations of HO_2 and OH via rovibrational lines at 6638.2 ($2\nu_1$) and 3407.6 cm^{-1} (ν_1), respectively. Typical experiments recorded the time-dependent UV kinetic trace and the two IR kinetic traces simultaneously via absorbance following the excimer photolysis pulse. All three signals were digitized and averaged {60 shot averaging for the HO_2 self-reaction and ≥800 shot averaging for the reactions with $CH_3C(O)CH_2O_2$} while being recorded using NI LabVIEW software.

Nitrogen-purged aluminum boxes at each end of the flow tube behind the gas exit ports contained custom-coated, half-moon-shaped, Herriot mirrors (Rocky Mountain Instrument Co.). The pulsed photolysis beam and continuous collimated broadband UV light from a laser-driven light source (Energetiq EQ-99XFC) entered and exited the cell above and below these mirrors to each make a single counterpropagating pass through the cell. The UV light was then isolated from the excimer beam outside the flow cell using dichroic mirrors and dispersed using a monochromator (Acton Research Corporation Spectra Pro-300i, 1200 grooves/mm) slit width ∼160 μm) coupled to a photomultiplier tube (EMI 9781A). The UV absorption path length was determined empirically to be 148 ± 10 cm long by measuring Cl_2 absorption at 320 nm ($\sigma_{Cl2} = 2.37 \times 10^{-19}$ cm^2).[39]

The two IR lasers, each wavelength-modulated at 6.8 MHz, entered the cell through a hole in one of the mirrors and each made 30 passes through the cell in a Herriot optical arrangement resulting in a total IR effective path length of approximately 27 meters. The IR beams exited the cell through the same hole that they entered and were detected independently after being separated by dichroic optics using an indium gallium arsenide detector (InGaAs, New Focus 1811) and a liquid nitrogen-cooled indium antimonide detector (InSb, IR Associates IS-0.25) for the near- and MIR wavelengths, respectively. The signals were demodulated at twice the modulation frequency (WMS, 2f-heterodyne detection, 13.6 MHz) and amplified by a factor of 200. The normalized noise-equivalent sensitivity concentrations for the detection of HO_2 and OH radicals were on the order of 10^8 molecule cm^{-3} $Hz^{-1/2}$ (10^9 molecule cm^{-3} for typical experiments). Calibration experiments determining the conversion factor between the 2f signals and the absolute HO_2 and OH concentrations were conducted daily at room temperature (see the Supporting Information from our previous publication[18] for further details).

2.4. Analysis of Experimental Data. The data used to determine kinetics parameters and the equilibrium constant/rate enhancement effects from CH_3OH adduct formation on R4 for the HO_2-self-reaction were fit using a Python-based kinetics modeling algorithm[41] that included the reactions from Table 1. The rate enhancement of R4 by radical adducts formed from the reaction of HO_2 with CH_3OH required only the NIR probe operating under WMS conditions to measure the loss of species due to diffusion, determine the starting radical concentrations, and measure the kinetic decay of the HO_2 reactant. The UVA probe {σ_λ(225 nm) = 2.88×10^{-18} cm^2 for HO_2 absorbance, with correction for H_2O_2 product absorbance at 225 nm[42]} was used only to calibrate the NIR laser absorbance. The equilibrium constant of R3, $K_{c,X}$, for X =

Table 1. Chemical Mechanism Used in Fitting Kinetics Data for the HO_2 Self-Reaction Data[a]

reaction number	chemical reaction	rate coefficient (cm^3 $molecule^{-1}$ s^{-1})
R6	$Cl + CH_3OH \rightarrow CH_2OH + HCl$	5.5×10^{-11}
R7	$CH_2OH + O_2 \rightarrow HO_2 + CH_2O$	9.1×10^{-12}
R4	$HO_2 + HO_2 \rightarrow H_2O_2 + O_2$	this work
	$Cl + HO_2 \rightarrow OH + ClO$	$3.6 \times 10^{-11}\exp(-375/T)$
	$\rightarrow O_2 + HCl$	$1.4 \times 10^{-11}\exp(270/T)$
	$HO_2 + CH_2O \rightarrow HOCH_2O_2$	$6.7 \times 10^{-15}\exp(-600/T)$

[a]Rate coefficients are taken from the recommended values in the JPL Data Evaluation 19-5;[42] R4 is the exception, which is from this work.

https://doi.org/10.1021/acs.jpca.3c03660
J. Phys. Chem. A 2023, 127, 7772−7792

CH_3OH was measured at 100 Torr over the temperature range T = 220−280 K, where

$$K_{c,X} = \frac{[HO_2 \cdot X]_{eq}}{[HO_2]_{eq}[X]_{eq}} \quad \text{(E2)}$$

and the kinetics parameters related to R4 were determined over the range T = 220−296 K. Within this temperature regime, only the lower CH_3OH concentrations (where linear regression fits well-represented the kinetic data) were used to exclude higher-order effects on the kinetics.

Experiments involving the $CH_3C(O)CH_2O_2$ radical were more complex and used the kinetics mechanism and fitting algorithm reported by Zuraski et al.[18] in the room-temperature measurement for this same chemistry with temperature-dependent rate coefficients and branching ratios from references included therein. Temperatures below 270 K were not used due to an observed increase in absorption in the UV kinetic trace ascribed to possible aerosol formation. Additional reactions suggested to be important for this chemical mechanism in the recent work by Assali and Fittschen[28] were tested in a sensitivity analysis but were not found to be relevant under our experimental conditions (see the Supporting Information). For R1 and R2, the $CH_3C(O)CH_2O_2$, HO_2, and OH kinetic data were fit simultaneously using a Levenberg−Marquardt algorithm[40,43,44] to optimize the kinetic rate coefficients, branching fractions, and rate enhancement terms for R4. Consistent with the room-temperature analysis, the fits were iterated 1000 times per experimental run following a Markov Chain Monte Carlo (MCMC) algorithm. This method randomly sampled all parameters and systematic uncertainties (reaction rate coefficients and branching fractions, concentrations, calibration constants, cell path length, Poisson counting in the data, and absorption cross sections) within each respective uncertainty. From this method, the value and uncertainty of each fitted parameter were determined from the geometric mean and full width at half-maximum (σ) of its resulting distribution (uncertainties reported as 2σ unless otherwise stated). Calculation of the geometric mean to constrain the peak value of the Gaussian fit was used to avoid the misrepresentation of the median value of the MCMC outputs (otherwise under- or over-estimated by the arithmetic mean) due to the asymmetry of the histogram distributions.[45] The $CH_3C(O)CH_2O_2$ self-reaction, R2, data were analyzed first, where the fitting algorithm determined the R2 reaction rate coefficient and branching fractions. These results were then incorporated into the R1 analysis, where the fitting algorithm was used to determine the R1 rate coefficient, branching fractions, and R4 enhancement term for the $CH_3C(O)CH_3$ precursor.

3. RESULTS

3.1. $CH_3C(O)CH_2O_2$ + $CH_3C(O)CH_2O_2$. Experiments monitoring the $CH_3C(O)CH_2O_2$ self-reaction, R2, simultaneously observed the $CH_3C(O)CH_2O_2$ reactant radicals and the HO_2 and OH product species that are generated from secondary chemistry following the subsequent alkoxy channel, R2b. The $CH_3C(O)CH_2O$ product rapidly decomposes to acetyl, CH_3CO, which undergoes O_2 addition to form acetyl peroxy, OH, and HO_2.[18] Figure 1 shows the observed kinetics for $CH_3C(O)CH_2O_2$ for T = 270−330 K at P = 100 Torr.

Representative fits for $[CH_3C(O)CH_2O_2]$, $[HO_2]$, and [OH] kinetics traces for T = 330 K are shown in Figure 2.

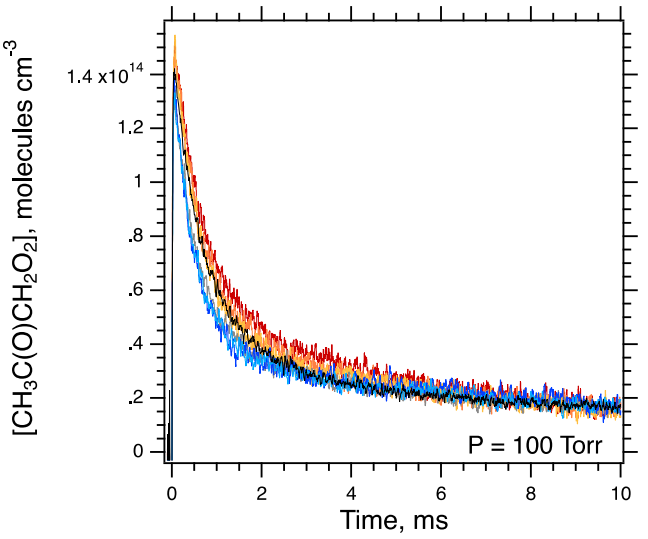

Figure 1. Acetonyl peroxy kinetics following the acetonyl peroxy self-reaction at T(K) = 330 (red), 320 (orange), 310 (yellow), 290 (gray), 280 (cyan), and 270 (blue). Experimental results from Zuraski et al.[18] for the acetonyl peroxy self-reaction under similar conditions at T = 298 K are shown in black. Reactant concentrations were approximately 1.5 × 10^{14}, 3.3 × 10^{16}, and 1.6 × 10^{18} molecule cm^{-3} for $[Cl]_0$, $[CH_3C(O)CH_3]_0$, and $[O_2]_0$, respectively.

For each temperature used over the range considered, the resulting distributions from the MCMC simulations for the rate coefficient k_2 and the branching fraction k_{2b}/k_2 are shown in Figure 3. The geometric mean values and uncertainties derived from the Gaussian fits for each temperature are given in Table 2. At T = 270, 280, and 290 K, the branching fraction, k_{2b}/k_2, showed bimodal distributions that may indicate that the fits are no longer constrained sufficiently to accurately determine the branching fraction or that the model is not accurately representing all of the OH and HO_2 production and loss channels. Increasing the number of iterations in the MCMC calculations did not resolve the observed asymmetry in the distributions. The branching fractions centering on the lower values for T = 270−290 K have broader (higher uncertainty) distributions and are inconsistent with the trend observed at the higher temperature values. Therefore, the distributions with the higher-value branching fractions are considered in this work to represent the reaction kinetics and are reported in Table 2 (see the Supporting Information for further discussion and numerical values for the other distributions).

Figure 4 shows the weighted fits to the outputs of both the k_2 and k_{2b}/k_2, which are inversely related to temperature. The fit in the Arrhenius plot (Figure 4a) for the rate coefficient, k_2, represents the rate parameters: A = $(1.5^{+0.3}_{-0.4})$ × 10^{-13} cm^3 $molecule^{-1}$ s^{-1} and E_a/R = −996 ± 334 K. The branching fraction, k_{2b}/k_2, follows the temperature-dependent expression: k_{2b}/k_2 = (2.27 ± 0.62) − [(6.35 ± 2.06) × 10^{-3}] T(K).

3.2. $CH_3C(O)CH_2O_2$ + HO_2. Figure 5 shows representative kinetics for $CH_3C(O)CH_2O_2$, HO_2, and the product OH for R1a at T = 270−330 K and P = 100 Torr. For clarity, only 270, 298, and 330 K are shown for the peroxy and OH kinetic traces. Figure 6 displays the outputs of the MCMC fits, and Table 3 gives the values for the geometric means of the MCMC outputs for the k_1 rate coefficients and the k_{1b}/k_1 branching fraction with their respective uncertainties derived from the Gaussian fits of the distributions at each temperature.

https://doi.org/10.1021/acs.jpca.3c03660
J. Phys. Chem. A 2023, 127, 7772−7792

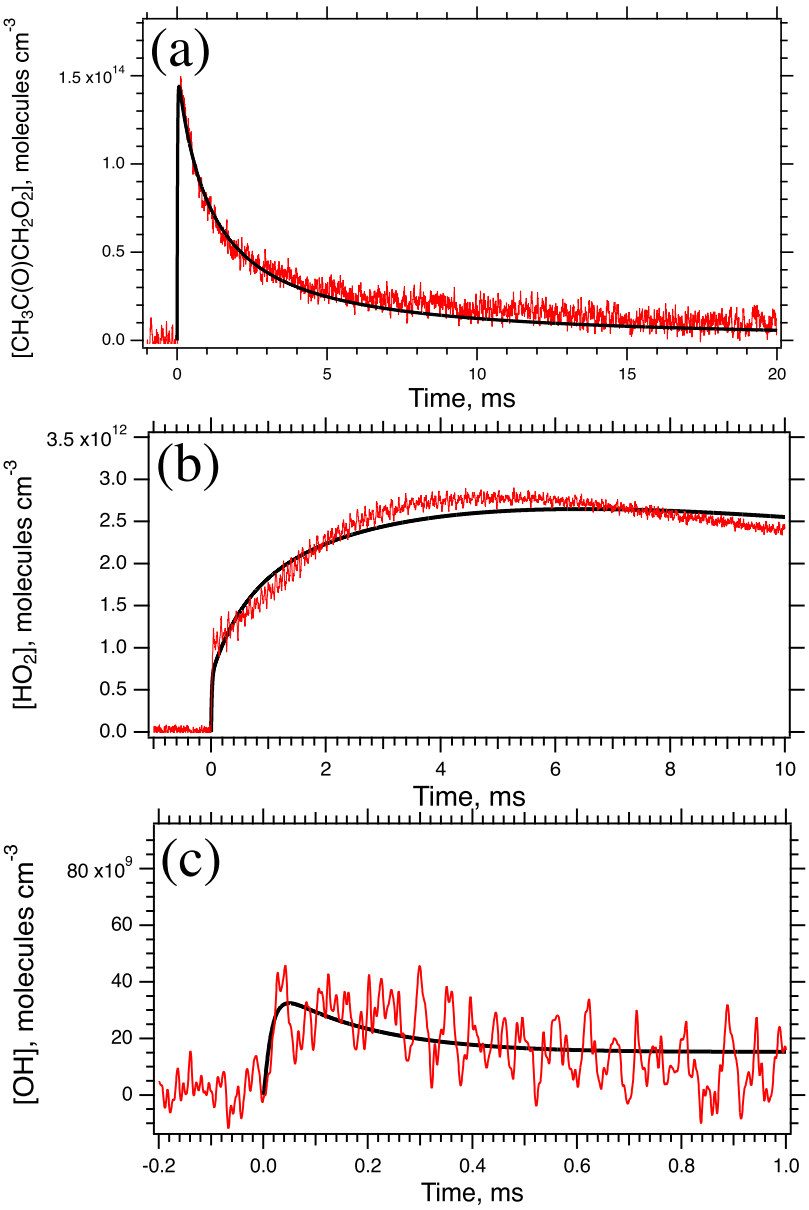

Figure 2. (a) Acetonyl peroxy, (b) HO_2, and (c) OH observed (red) kinetics following the acetonyl peroxy self-reaction at T = 330 K and P = 100 Torr. Simulations from the fit results are shown in black. The fits for the acetonylperoxy kinetics follow the primary reactant for the R2a reaction. OH and HO_2 fits are the results of secondary chemistry.

The inverse correlations between the temperature and k_{1a}, k_{1b}, and k_{1b}/k_1 are shown in Figure 7. The weighted fits in the Arrhenius plot were used to calculate the rate parameters: $A = (3.4^{+2.5}_{-1.5}) \times 10^{-13}$ cm^3 molecule^{-1} s^{-1} and $E_a/R = -547 \pm 415$ K for k_{1a} and $A = (6.23^{+15.3}_{-4.4}) \times 10^{-17}$ cm^3 molecule^{-1} s^{-1} and $E_a/R = -3100 \pm 870$ K for k_{1b}. The branching fraction, k_{1b}/k_1, follows the temperature-dependent expression: $k_{1b}/k_1 = (3.27 \pm 0.51) - [(9.6 \pm 1.7) \times 10^{-3}]\ T(\mathrm{K})$.

3.3. HO_2 Self-Reaction Rate Enhancement by Radical Adducts. *3.3.1. Temperature Dependence of the Equilibrium Constant for HO_2 + CH_3OH ⇌ HO_2·CH_3OH.* Following photolysis, the initial Cl atoms, $[Cl]_0$, were completely converted to HO_2. The total initial HO_2 concentration, $[HO_2]_0$, is expressed as

$$[HO_2]_0 = [HO_2]_{eq} + [HO_2 \cdot CH_3OH]_{eq} = [Cl]_0 \quad \text{(E3)}$$

where $[HO_2]_{eq}$ and $[HO_2 \cdot CH_3OH]_{eq}$ are the concentrations of the remaining HO_2 and the complex $HO_2 \cdot CH_3OH$, respectively, following the rapid equilibrium reaction

$$HO_2 + CH_3OH \rightleftharpoons HO_2 \cdot CH_3OH \quad \text{(R10)}$$

The equilibrium constants for R10 were determined at each temperature by measuring the loss of HO_2 in the first ~20−50 μs after photolysis using the NIR probe. This approach assumes that the timescale for reaching equilibrium is much shorter than that for HO_2 loss by R4. This assumption was validated by the observed drop in the peak HO_2 signal with increasing $[CH_3OH]_0$ (CH_3OH is in excess) at early times (t < 50 μs). Because the NIR probe only measures the amount of non-complexed HO_2, the observed difference in the peak $[HO_2]$ signal with various concentrations of CH_3OH provided an indirect measurement of the equilibrium concentration of the complex formed.

https://doi.org/10.1021/acs.jpca.3c03660
J. Phys. Chem. A 2023, 127, 7772−7792

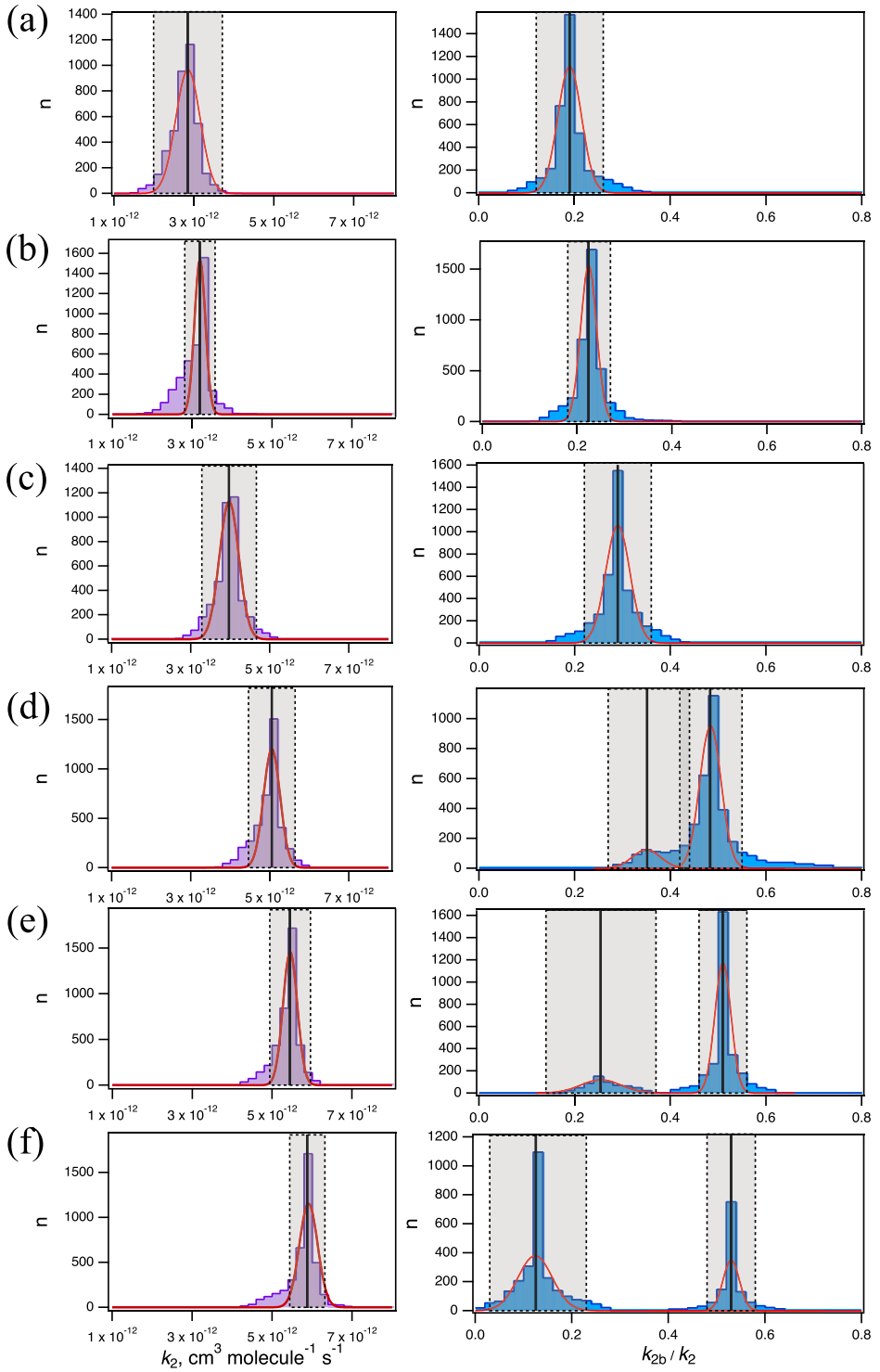

Figure 3. Histogram outputs from the MCMC simulations (4000 iterations per temperature) for T = (a) 330, (b) 320, (c) 310, (d) 290, (e) 280, and (f) 270 K. The left panels (purple) display the distributions of rate coefficients, k_2, and the right panels (blue) display the distributions of branching fractions, k_{2b}/k_2. Solid (black) vertical lines indicate the geometric means of the distributions. The uncertainties (2σ, gray shaded region) represent twice the full width at half-maximum of the (red) Gaussian fits.

Using the definition $\Delta[HO_2]_0 \equiv [HO_2]_0 - [HO_2]_{eq}$, and for the case of the CH_3OH precursor only, E2 can be written as

$$\frac{\Delta[HO_2]_0}{[HO_2]_{eq}} = K_{c,M}[CH_3OH]_0 \quad \text{(E4)}$$

$K_{c,M}$ is then determined from the slope of $\Delta[HO_2]_0/[HO_2]_{eq}$ as a function of $[CH_3OH]_0$. Figure 8 shows examples of the $[HO_2]$ decays obtained from the NIR probe at various $[CH_3OH]_0$ at T = 220 K. As shown in the Figure 8 inset, the data exhibited peak $[HO_2]$ signal drops immediately after photolysis (t < 50 μs), supporting the hypothesis that equilibrium of R10 is established rapidly. The magnitude of peak signal attenuation was positively correlated with $[CH_3OH]_0$, with the same initial radical concentrations

https://doi.org/10.1021/acs.jpca.3c03660
J. Phys. Chem. A 2023, 127, 7772−7792

Table 2. Results from the MCMC Simulations for the Acetonyl Peroxy Self-Reaction

T (K)	k_2, 10^{12} cm^3 molecule^{-1} s^{-1}	branching fraction to the alkoxy channel (R2b)
330 ± 1	2.85 ± 0.76	0.19 ± 0.07
320 ± 1	3.19 ± 0.38	0.23 ± 0.05
310 ± 1	3.97 ± 0.69	0.29 ± 0.07
298 ± 2[a]	4.8 ± 0.8	0.33 ± 0.13
290 ± 1	5.05 ± 0.59	0.48 ± 0.06
280 ± 1	5.45 ± 0.51	0.51 ± 0.05
270 ± 1	5.88 ± 0.44	0.53 ± 0.05

[a]Values from Zuraski et al.[17]

being used for each run. The extrapolated value of $[HO_2]$ at t = 0 s was taken to be $[HO_2]_{eq}$. Uncertainties in the measured values of $[HO_2]_{eq}$ include the random errors in the kinetics fits.

To determine $[HO_2]_0$ for each experiment, E4 can be rearranged using the definition of $\Delta[HO_2]_0$ to obtain

$$\frac{1}{[HO_2]_{eq}} = \frac{1}{[HO_2]_0} + \frac{K_{c,M}}{[HO_2]_0}[CH_3OH]_0 \quad \text{(E5)}$$

$[HO_2]_0$ is then derived from the y-intercept of a plot of $1/[HO_2]_{eq}$ versus $[CH_3OH]_0$. Figure 9a shows an example of such a plot for T = 250 K with a linear regression fit to obtain $1/[HO_2]_0$.

Multiple datasets were combined on a common scale by plotting $\Delta[HO_2]_0/[HO_2]_{eq}$ as a function of $[CH_3OH]_0$, as shown in Figure 9b. $K_{c,M}$ at each temperature was derived from the slope of the weighted linear regression fit to the data, which are given in Table 4 alongside the corresponding $K_{P,M}$ values. The data obtained at and above T = 290 K did not show evidence of complexation within experimental uncertainty; thus, $K_{c,M}$ was not determined at the higher temperatures.

Figure 10 shows the van't Hoff plot of R ln $K_{P,M}$ versus inverse temperature. The resulting second law fit to the data yielded $\Delta_r H^\circ_{250K}$ = −38.6 ± 3.3 kJ mol^{-1} from the slope and $\Delta_r S^\circ_{250K}$ = −110.5 ± 13.2 J mol^{-1} K^{-1} from the y-intercept (2σ uncertainties), where T = 250 K is the midpoint of the temperature range. These experimental values agree with the theoretically calculated values of $\Delta_r H^\circ_{245K}$ = −36.8 kJ mol^{-1} and $\Delta_r S^\circ_{245K}$ = −106 J mol^{-1} K^{-1}.[34] Given the very small change in $\Delta_r S^\circ_T$ with temperature,[35] this calculated value was used for $\Delta_r S^\circ_{250K}$ as fixed to carry out a non-weighted third-law van't Hoff plot yielding $\Delta_r H^\circ_{250K}$ = −37.5 ± 0.25 kJ mol^{-1} (2σ uncertainty). Both the second and third law fits are shown in Figure 10.

From the reaction thermodynamics, the enthalpy of formation and absolute entropy of the H-bonded complex can be calculated at T = 250 K using the accepted values of these quantities for the reactants, HO_2 and CH_3OH, and their heat capacities along with those for the associated element species.[42,46] The values determined for $HO_2{\cdot}CH_3OH$ are $\Delta_f H^\circ_{250K}$ = −225 ± 3.4 kJ mol^{-1} and S°_{250K} = 348 ± 13.2 J mol^{-1} K^{-1} using the second-law values. The equivalent values using the third-law results are $\Delta_f H^\circ_{250K}$ = −223.7 ± 0.74 kJ mol^{-1} and S°_{250K} = 352 J mol^{-1} K^{-1}. The uncertainty is not shown for S°_{250K} because the uncertainty in the literature value[43] for $S^\circ_{250K}(HO_2)$ is not clearly given. Uncertainties listed in all other cases are 2σ.

3.3.2. Rate Enhancement of the HO_2 Self-Reaction by CH_3OH. As described generally in Section 1 (R3, R5a, and R5b), the H-bonded adduct, $HO_2{\cdot}CH_3OH$, formed from the reaction of HO_2 with CH_3OH, impacts the rate of the HO_2 self-reaction (R4) through the following chaperone mechanism

$$HO_2 + CH_3OH \rightleftharpoons HO_2{\cdot}CH_3OH \quad \text{(R11)}$$

$$HO_2 + HO_2{\cdot}CH_3OH \rightarrow H_2O_2 + O_2 + CH_3OH \quad \text{(R12)}$$

$$HO_2{\cdot}CH_3OH + HO_2{\cdot}CH_3OH \rightarrow H_2O_2 + O_2 + 2\,CH_3OH \quad \text{(R13)}$$

Combining these reactions with the HO_2 self-reaction, R4, and the fact that R11 is a fast pre-equilibrium, the rate law for HO_2, when measuring only $[HO_2]$ via the IR signal, is found[35] to be

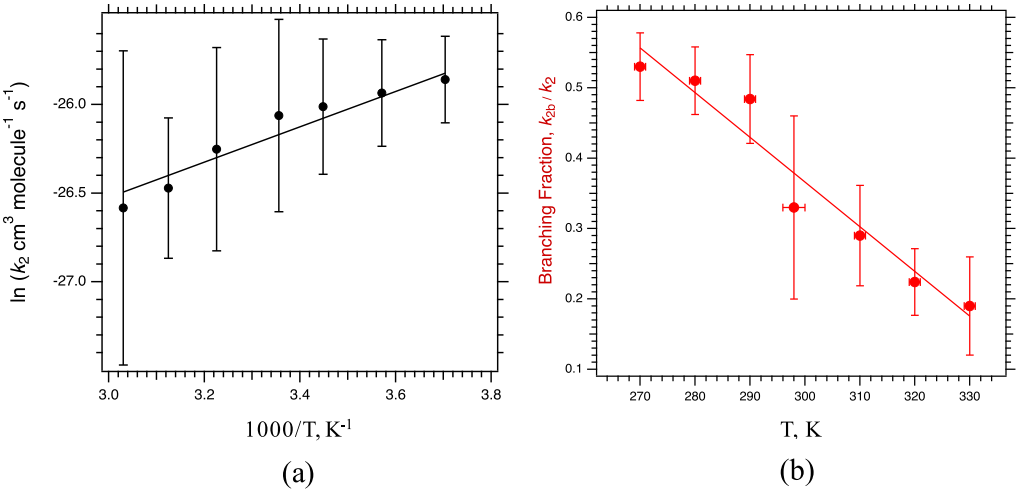

Figure 4. (a) Arrhenius plot for the temperature dependence of k_2 (black, filled circles) and (b) linear temperature dependence (red, filled circles) for the branching fraction, k_{2b}/k_2. The linear regression fit weighted by the uncertainty (black line) in (a) represents the parameters ln(A, cm^3 molecule^{-1} s^{-1}) = −29.51 ± 4.66 and E_a/R = −996 ± 334 K. The linear regression fit weighted by the uncertainty (red line) for the branching fraction gives the correlation, k_{2b}/k_2 = (2.27 ± 0.62) − [(6.35 ± 2.06) × 10^{-3}] T(K).

https://doi.org/10.1021/acs.jpca.3c03660
J. Phys. Chem. A 2023, 127, 7772−7792

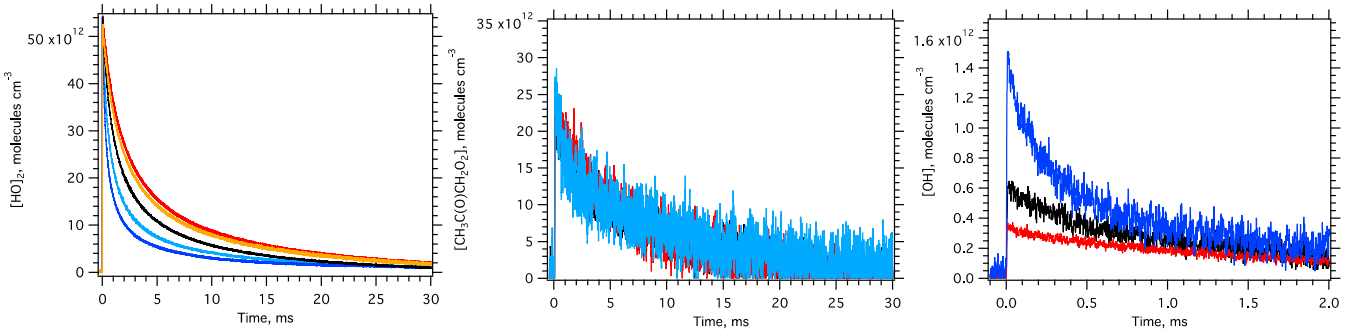

Figure 5. Time-dependent (a) $[HO_2]$, (b) $[CH_3C(O)CH_2O_2]$, and (c) product [OH] following the $CH_3C(O)CH_2O_2 + HO_2$ reaction at T(K) = 330 (red), 320 (orange), 310 (yellow), 290 (gray), 280 (cyan), and 270 (blue). For clarity, only the 330, 298, and 270 K data are shown for $[CH_3C(O)CH_2O_2]$ and [OH] due to the reduced S/N and lower product concentrations, respectively. Reactant concentrations were approximately 1.5×10^{14}, 3.3×10^{16}, and 1.6×10^{18} molecule cm^{-3} for $[Cl]_0$, $[CH_3C(O)CH_3]_0$, and $[O_2]_0$, respectively.

$$\frac{d[HO_2]}{dt} = -2\left(\frac{k_4 + k_{12}K_{C,M}[CH_3OH] + k_{13}K_{C,M}^2[CH_3OH]^2}{1 + K_{C,M}[CH_3OH]}\right)[HO_2]^2 \quad \text{(E6)}$$

$$= -2\,(k_{4,obs})[HO_2]^2 \quad \text{(E7)}$$

where $K_{c,M}$ is the equilibrium constant for R11. When $K_{C,M}[CH_3OH] \ll 1$, the denominator can be expanded, and taking the first three terms

$$k_{obs} = k_{4,M} + (k_{12} - k_4)K_{C,M}[CH_3OH] + (k_{13} - k_{12} + k_4)K_{C,M}^2[CH_3OH]^2 \quad \text{(E8)}$$

$$= k_{4,M} + k''_{4,M}\,[CH_3OH] + k'''_{4,M}\,[CH_3OH]^2 \quad \text{(E9)}$$

As expressed in E9, the observed second-order rate coefficient is linear with respect to $[CH_3OH]$ for small values $K_{c,M}$ (higher T) with the proportionality constant given by the rate enhancement term, $k''_{4,M}$. At higher values of $K_{c,M}$ (lower T), curvature may be observed due to the quadratic term.

Figure 11 shows a plot of $k_{4,obs}$ versus $[CH_3OH]_0$ for each temperature studied. Linearity in the data is observed at $T >$ 250 K for all measured $[CH_3OH]_0$, whereas nonlinear curvature is observed at the higher $[CH_3OH]_0$ for $T \leq 250$ K. Linear regression of the data points over the ranges of $[CH_3OH]_0$ that were observed to be linear (see Table 5), weighted by the uncertainties in $[CH_3OH]$ (~5%) and the fitted values of $k_{4,obs}$ (random error ~1−3%), was performed to obtain k_4 and $k''_{4,M}$ from the y-intercepts and slopes, respectively. In addition, the full range of $[CH_3OH]_0$ measurements taken at $T \leq 250$ K was fit with a 3-term polynomial. The third-order term gives an estimate for $k'''_{4,M}$. Table 5 lists the fitted values of k_4 and $k''_{4,M}$ at each temperature over the range of $[CH_3OH]_0$ found to be linear as well as the fitted values of $k_{4,M}$, and $k''_{4,M}$ and $k'''_{4,M}$ (for T = 220−250 K) over the full range of $[CH_3OH]_0$ when the polynomial fit was used. Agreement is observed for the k_4 and $k''_{4,M}$ terms found by both the truncated linear fits and the 3-term polynomial fits for T = 220−250 K. (It is also possible that the formation of higher-order clusters, $(HO_2)_n(CH_3OH)_m$, could lead to additional rate enhancements for $k_{4,obs}$, but that is not addressed in our work here.)

The Arrhenius plot of our fit values for the linear range of $k''_{4,M}$ is given in Figure 12 with a weighted fit by the uncertainties. Our expression for $k''_{4,M}$ at 100 Torr in N_2 with 2σ uncertainties ($\ln A''_{4,M} = -81.91 \pm 1.0$; $E_a/R = -4700 \pm 255$ K) was determined to be

$$k''_{4,M} = (2.7^{+4.7}_{-1.7}) \times 10^{-36}\exp[(4700 \pm 255)/T]\ cm^6\ molecule^{-2}\ s^{-1} \quad \text{(E10)}$$

The results from Christensen et al.[35] and Tang et al.[36] are also shown in Figure 12 over the respective temperature ranges studied, which are discussed further in Section 4. Note that the error bars in Figure 12 for Tang et al. are only from statistical fits, whereas our error bars include propagated experimental uncertainties.

3.3.3. Temperature Dependence of the HO_2 Self-Reaction Kinetic Rate Coefficient. The k_4 values given in Table 5 allow us to determine the temperature dependence of the$_2$ self-reaction in the absense of any precursor to compare our results to previous studies. The Arrhenius plot of k_4 at 100 Torr is given in Figure 13a, again shown in comparison to work by Tang et al.[36] and Christensen et al.[35] As before, the error bars for the values from Tang et al. error bars in Figure 13 result only from statistical fits, whereas our error bars include propagated experimental uncertainties.

A linear regression fit weighted by the uncertainties to our data yielded the Arrhenius parameters $\ln A_{4,M} = -28.73 \pm 0.27$ and $E_a/R = -507 \pm 76$ K resulting in the expression

$$k_4 = (3.34^{+1.04}_{-0.80}) \times 10^{-13}\exp[(507 \pm 76)/T]\ cm^3\ molecule^{-1}\ s^{-1} \quad \text{(E11)}$$

where the uncertainties are 2σ. Given that Tang et al. carried out their experiments at a different pressure (30 Torr) than this work, the bimolecular rate coefficients for the HO_2 self-reaction (E1), $k_{4,bi}$, were determined for both studies using the JPL recommended value[43] of $k_{4,ter} = 2.1 \times 10^{-33}$ [M] exp (920/T) for the termolecular reaction (E1). These bimolecular rate coefficients result in a better comparison between these two studies which is depicted in Figure 13b. From our results, the Arrhenius parameters for $k_{4,bi}$ were determined to be $A_{4,bi} = (3.47^{+1.19}_{-0.88}) \times 10^{-13}$ cm^3 $molecule^{-1}$ s^{-1} and $E_a/R = -468 \pm 82$ K (2σ uncertainties). The comparison is presented in Section 4.

https://doi.org/10.1021/acs.jpca.3c03660
J. Phys. Chem. A 2023, 127, 7772−7792

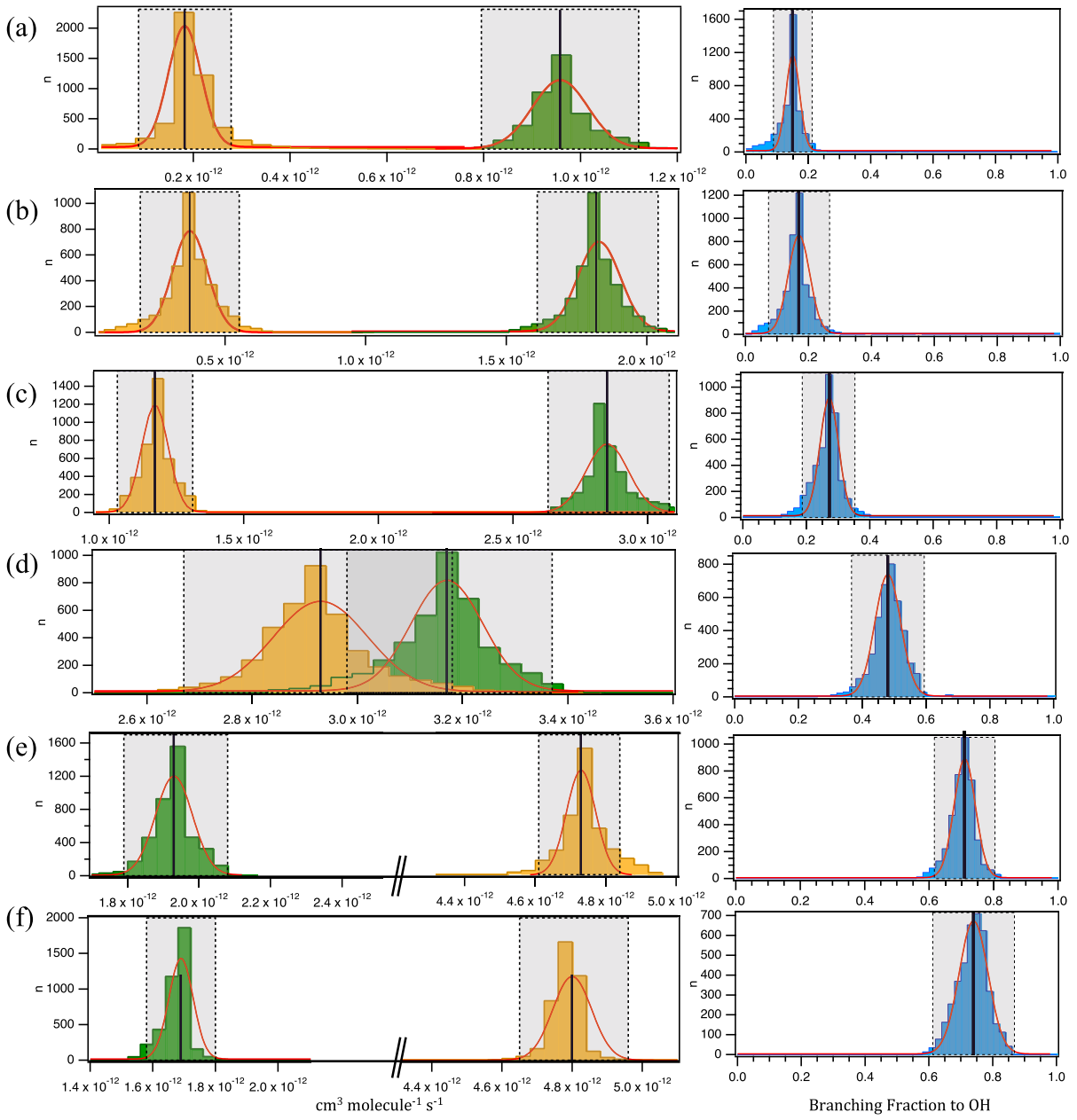

Figure 6. Histogram outputs from the MCMC simulations (4000 iterations) for (green) k_{1a}, (yellow) k_{1b}, and the (blue) branching fraction, k_{1b}/k_1 at T = (a) 330, (b) 320, (c) 310, (d) 290, (e) 280, and (f) 270 K. Solid (black) vertical lines indicate the geometric means of the distributions. The uncertainties (2σ, gray shaded region) represent twice the full width at half-maximum of the (red) Gaussian fits.

Table 3. Results from the MCMC Simulations for the $CH_3C(O)CH_2O_2$ + HO_2 Reaction[a]

T, K	k_{1a} 10^{12} cm^3 molecule^{-1} s^{-1}	k_{1b} 10^{12} cm^3 molecule^{-1} s^{-1}	branching fraction for OH channel (R1b)
330 ± 1	0.96 ± 0.16	0.18 ± 0.10	0.16 ± 0.03
320 ± 1	1.83 ± 0.21	0.37 ± 0.18	0.17 ± 0.05
310 ± 1	2.85 ± 0.22	1.17 ± 0.14	0.29 ± 0.04
298 ± 2[b]	3.85 ± 0.22	1.65 ± 0.50	0.30 ± 0.04
290 ± 1	3.17 ± 0.19	2.93 ± 0.25	0.48 ± 0.08
280 ± 1	1.93 ± 0.15	4.73 ± 0.12	0.71 ± 0.05
270 ± 1	1.69 ± 0.11	4.80 ± 0.16	0.74 ± 0.10

[a]Uncertainties are 2σ. [b]Values from Zuraski et al.[18]

3.3.4. Temperature Dependence of Rate Enhancement of the HO_2 Self-Reaction by $CH_3C(O)CH_3$. As shown in our room-temperature study,[18] $CH_3C(O)CH_3$ increases the reaction rate of the HO_2 self-reaction via an analogous chaperone mechanism (R14–R16) but with a higher enhancement term compared to that of CH_3OH.

$$HO_2 + CH_3C(O)CH_3 \rightleftharpoons HO_2{\cdot}CH_3C(O)CH_3 \qquad \text{(R14)}$$

https://doi.org/10.1021/acs.jpca.3c03660
J. Phys. Chem. A 2023, 127, 7772−7792

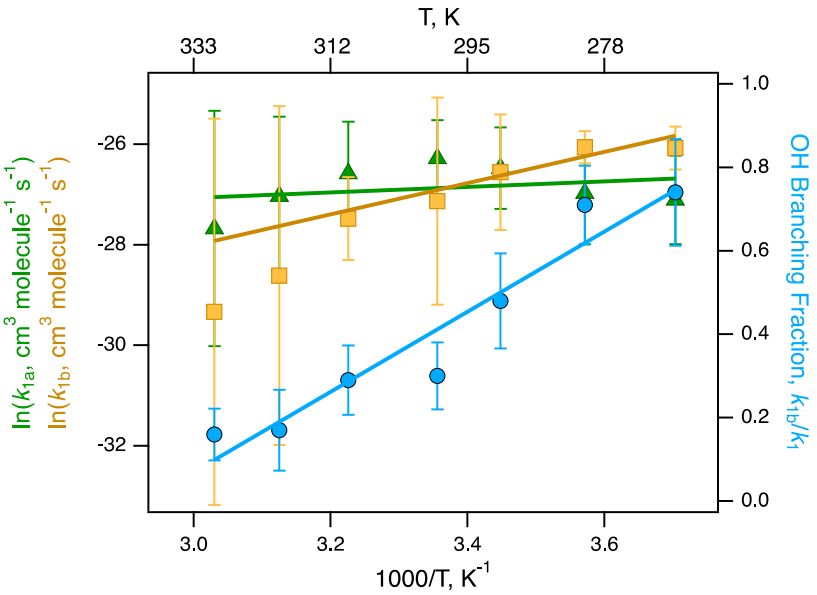

Figure 7. (left axis) Arrhenius plot for the temperature dependence of k_{1a} and k_{1b} as well as (right axis) the linear temperature dependence for the branching fraction to the OH channel, k_{1b}/k_1. The weighted fits in the Arrhenius plot determined the rate parameters: $\ln(A, \text{cm}^3\ \text{molecule}^{-1}\ \text{s}^{-1}) = (-28.71 \pm 0.56) \times 10^{-13}$ and $E_a/R = -547 \pm 415\ \text{K}^{-1}$ for k_{1a} and $\ln(A, \text{cm}^3\ \text{molecule}^{-1}\ \text{s}^{-1}) = (-37.32 \pm 1.24)$ and $E_a/R = -3100 \pm 870\ \text{K}^{-1}$ for k_{1b}. The branching fraction, k_{1b}/k_1, follows the temperature-dependent expression (blue line): $k_{1b}/k_1 = (3.27 \pm 0.51) - [(9.6 \pm 1.7) \times 10^{-3}]\ T(\text{K})$.

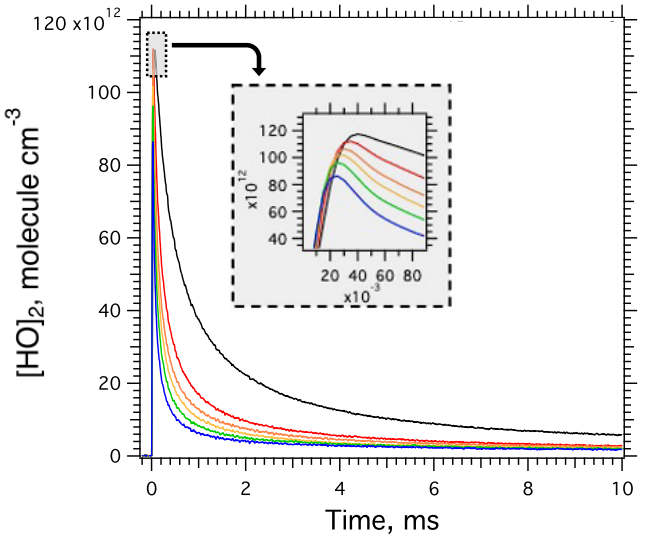

Figure 8. Example data of $[HO_2]$ decay curves at $T = 220$ K and $P = 100$ Torr. The inset shows an expanded view of the peak signal.

$$HO_2 + HO_2{\cdot}CH_3C(O)CH_3 \rightarrow H_2O_2 + O_2 + CH_3C(O)CH_3 \quad \text{(R15)}$$

$$HO_2{\cdot}CH_3C(O)CH_3 + HO_2{\cdot}CH_3C(O)CH_3 \rightarrow H_2O_2 + O_2 + 2\,CH_3C(O)CH_3 \quad \text{(R16)}$$

This increase in rate is due in part to the increased concentration of the $CH_3C(O)CH_3$ H-bonded complex, $HO_2{\cdot}CH_3C(O)CH_3$, because of the larger equilibrium constant $K_{c,A}$ (16×10^{-19} cm^3 molecule^{-1}) compared to that of $K_{c,M}$ (4.0×10^{-19} cm^3 molecule^{-1}) at 298 K and 100 Torr, where $K_{c,A}$ is the equilibrium constant for R14. The $CH_3C(O)CH_3$ chaperone enhancement term at 298 K and 100 Torr was measured to be $k''_{4,A} = (4.0 \pm 0.2) \times 10^{-29}$ cm^6 molecule^{-2} s^{-1}.[18] Using our expression for the CH_3OH adduct given in Section 3.3.2, extrapolating to $T = 298$ K, $k''_{4,M} = 1.7 \times 10^{-29}$ cm^6 molecule^{-2} s^{-1}, which further decreases the chaperone enhancement compared to $CH_3C(O)CH_3$ by a factor of 2.4.

At lower temperatures, both the CH_3OH and $CH_3C(O)CH_3$ H-bonded adducts with HO_2 are formed when both precursors are present. The temperature dependence of $K_{c,A}$ for the formation of $HO_2{\cdot}CH_3C(O)CH_3$ was determined previously[38] and that of $K_{c,M}$ is given in Section 3.3.1. The large concentrations of both adducts at lower temperatures result in an observable combined chaperone effect. The observed rate constant for the HO_2 self-reaction, $k_{4,obs}$, then becomes $k_4 + k''_{4,M}[CH_3OH] + k''_{4,A}[CH_3C(O)CH_3]$ where M and A are used to designate CH_3OH and $CH_3C(O)CH_3$ enhancement, respectively. The $CH_3C(O)CH_3$ chaperone enhancement term, $k''_{4,A}$, is a similar combination of rate coefficients and $K_{c,A}$, the equilibrium constant for R3 with X = $CH_3C(O)CH_3$, as shown in E8 for $[CH_3OH]$

$$k''_{4,A} = (k_{15} - k_4)K_{C,A} \quad \text{(E12)}$$

where only the first two terms of the expansion E9 have been included.

To determine $k''_{4,A}$ at a lower temperature, $k_{4,obs}$ was determined simultaneously with k_1, k_2, and the branching fractions as described above at a fixed $[CH_3OH]$ for several $CH_3C(O)CH_3$ concentrations. The rate coefficient $k_{4,obs}$ was then plotted as a function of $[CH_3C(O)CH_3]$, yielding a slope of $k''_{4,A}$ and intercept of $(k_4 + k''_{4,M}[CH_3OH] = k_{4,M})$. The temperature dependence of $k''_{4,A}$ was determined by measuring $k_{4,obs}$ at several temperatures over the range of $T = 298$–270 K. Several fixed values of $[CH_3OH]$ were used at each selected temperature to check for any unexpected systematic error due to the change in this concentration.

The data for $T = 290$–270 K, which included three experimental runs with different fixed $[CH_3OH]$ at each of these temperatures, are presented in Figure 14 along with the linear regression fit for each experiment. The $[CH_3C(O)CH_3]$

https://doi.org/10.1021/acs.jpca.3c03660
J. Phys. Chem. A 2023, 127, 7772−7792

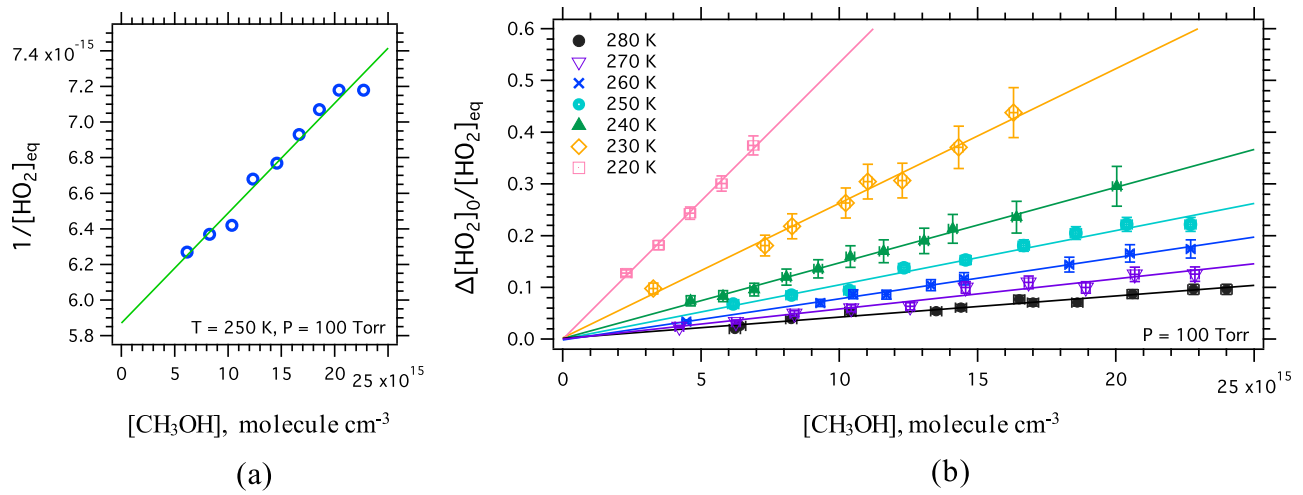

Figure 9. (a) $1/[HO_2]_{eq}$ vs $[CH_3OH]$ at T = 250 K and P = 100 Torr. The data points (blue circles) were fit using linear regression (green line) to determine $[HO_2]_0$ from the inverse of the y-intercept. (b) $\Delta[HO_2]_0/[HO_2]_{eq}$ vs $[CH_3OH]$ plots for T = 220−280 K. The data points at each T were fit using an inverse-variance-weighted linear regression to determine $K_{c,M}(T)$ from the slopes.

Table 4. Temperature-Dependent $K_{c,M}$ and $K_{P,M}$ at 100 Torr[a]

T(K)	$K_{c,M}$ (10^{18} cm^3 molecule^{-1})	$K_{P,M}$ (atm^{-1})
280 ± 1	0.90 ± 0.26	23.6 ± 6.8
270 ± 1	1.60 ± 0.48	43.5 ± 13
260 ± 1	3.91 ± 0.24	110.4 ± 6.8
250 ± 1	8.27 ± 0.7	242.8 ± 21
240 ± 1	16.1 ± 0.3	492.3 ± 9.2
230 ± 1	29.2 ± 1.1	931.7 ± 35
220 ± 1	64.4 ± 1.7	2148.3 ± 57

[a]Uncertainties are 2σ.

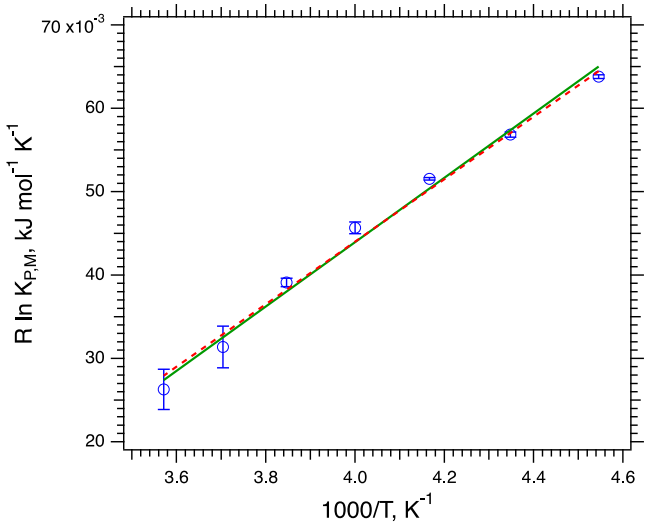

Figure 10. van't Hoff plot of R ln $K_{P,M}$ versus 1000/T (blue circles). The second-law non-weighted linear regression fit (green line) has an R^2 value of 0.9911. Coefficient values ± 2σ from the fit (in the format $R \ln K_{P,M} = \frac{\Delta_r H^\circ_{250K}}{T} - \Delta_r S^\circ_{250K}$) where $\Delta_r S^\circ_{250K}$ = −110.5 ± 13.2 J mol^{-1} K^{-1} and $\Delta_r H^\circ_{250K}$ = −38.6 ± 3.3 kJ mol^{-1}. The third-law non-weighted linear regression fit (red, dashed line) using the calculated $\Delta_r S^\circ_{250K}$ = −106 J mol^{-1} K^{-1} has an R^2 value of 0.99993 and $\Delta_r H^\circ_{250K}$ = −37.5 ± 0.25 kJ mol^{-1}.

was varied from (1.2−3.5) × 10^{16} molecule cm^{-3}. Table 6 shows the results from the linear regressions yielding $k''_{4,A}$, which varies by a factor of 5 over this temperature range (1.1−5.2 × 10^{-28} cm^6 molecule^{-2} s^{-1}). These chaperone enhancement terms are larger than comparable values for the CH_3OH adduct, 0.28−0.98 × 10^{-28} cm^6 molecule^{-2} s^{-1}. The $[CH_3C(O)CH_3]$ = 0 intercepts, also reported in Table 6, represent the observed enhancement from only CH_3OH, $k_{4,M} = k_4 + k''_{4,M}[CH_3OH]$. This rate coefficient can also be calculated from our results given in Section 3.3.2 at each given temperature for the fixed value of $[CH_3OH]$. A good agreement is observed between the calculated $k_{4,M}$ values and the $k_{4,M}$ values determined by the intercept.

Figure 15 shows the Arrhenius plot for $k''_{4,A}$ including the room temperature value (4.0 ± 0.2) × 10^{-29} cm^6 molecule^{-2} s^{-1} from Zuraski et al.[18] The weighted linear regression fit represents the temperature-dependent rate expression: $k''_{4,A}$ = (5.0 × 10^{-38} − 1.4 × 10^{-41}) exp[(7396 ± 1172)/T] cm^6 molecule^{-2} s^{-1} (expressed as a 2σ interval.)

4. DISCUSSION

4.1. Acetonylperoxy Kinetics. This is the first study to measure the temperature dependence of the kinetics for the reaction between $CH_3C(O)CH_2O_2$ and HO_2 (R1a), and the $CH_3C(O)CH_2O_2$ self-reaction (R2a). In both R1a and R2a, the histogram distributions from the MCMC simulations were not symmetric and increasing the number of MCMC iterations did not improve the symmetry. The asymmetry in the distributions could arise from large asymmetric uncertainty in some of the chemistry involved in the reaction mechanism or the shape of the potential energy surface for the reaction having multiple channels with different barriers.

We report the overall rate coefficients for R2a and the branching fraction to the alkoxy channel, R2b/R2a. The rate coefficient shows an inverse temperature dependence where the rate coefficient approximately doubled when observed from 330 to 270 K. A bimodal distribution in the output of the MCMC simulations was observed for the branching fraction to the alkoxy channel, R2b/R2, for T = 270−290 K. For this reaction, HO_2 and OH are secondary products following the generation of the alkoxy species through the R2b channel. As our experiments do not observe the other two channels for R2, it is possible that the bimodal distributions observed at lower

https://doi.org/10.1021/acs.jpca.3c03660
J. Phys. Chem. A 2023, 127, 7772−7792

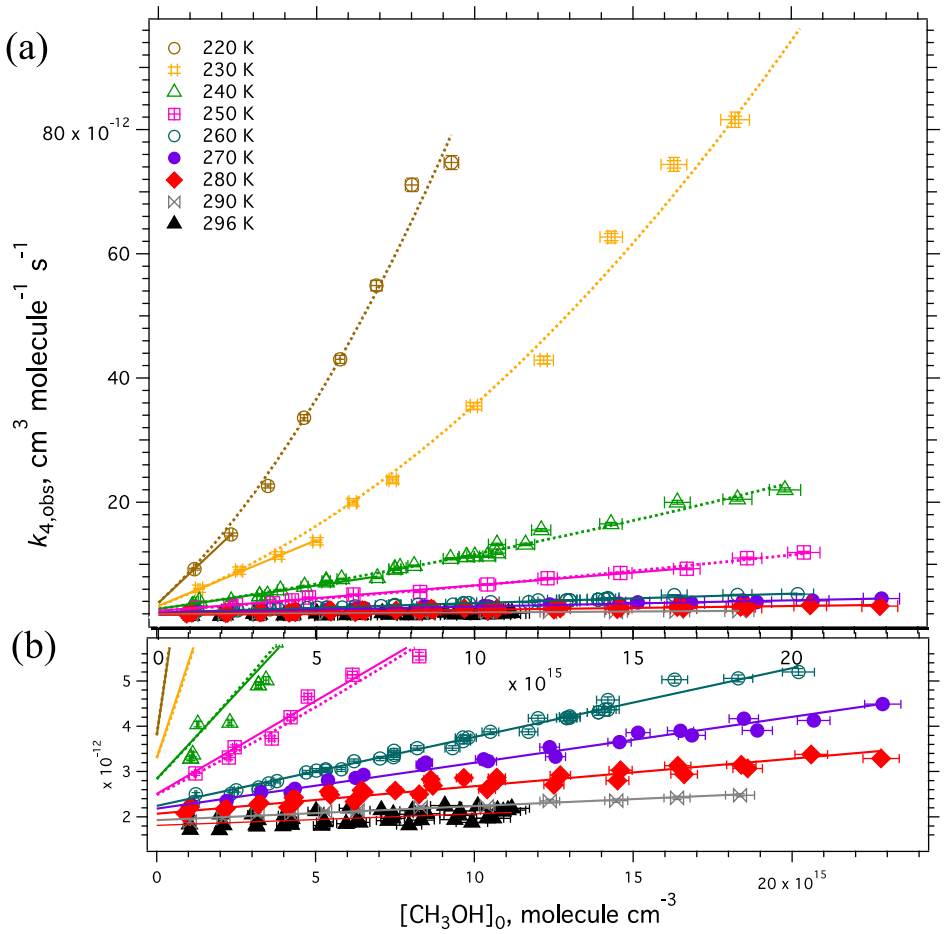

Figure 11. Observed HO_2 self-reaction rate coefficient, $k_{4,obs}$, as a function of $[CH_3OH]_0$. The data in (a) is shown in an expanded scale in (b). Linear regression fits (solid lines) are shown for the region of $[CH_3OH]_0$ that was linear and 3-term polynomial fits (dashed lines) are shown over the full $[CH_3OH]_0$ range for T = 220−250 K.

Table 5. Linear Regression Fit Values of k_4 and $k''_{4,M}$ at Each Temperature over the Range Where $[CH_3OH]_0$ Was Shown to Be Linear and 3-Term Polynomial Fit Parameters, k_4, $k''_{4,M}$, and $k'''_{4,M}$, for $T \leq 250$ K over the Full Range of $[CH_3OH]$ Measured[a]

	fit values for a linear range of $k_{4,obs}$			nonlinear fit values		
	highest $[CH_3OH]_0$ used in fit	k_4	$k''_{4,M}$	k_4	$k''_{4,M}$	$k'''_{4,M}$
T (K)	(10^{-15} molecule cm^{-3})	(10^{12} cm^3 s^{-1})	(10^{29} cm^6 s^{-1})	(10^{12} cm^3 s)	(10^{29} cm^6 s^{-1})	(10^{46} cm^9 s^{-1})
296 ± 2	11.2	1.81 ± 0.08	2.56 ± 1.12			
290 ± 1	18.4	1.93 ± 0.03	3.09 ± 0.33			
280 ± 1	22.8	2.07 ± 0.10	6.06 ± 0.89			
270 ± 1	22.9	2.18 ± 0.08	10.1 ± 0.68			
260 ± 1	20.2	2.24 ± 0.09	15.2 ± 0.9			
250 ± 1	16.7	2.51 ± 0.18	42.6 ± 2.2	2.49 ± 0.30	36.6 ± 7.8	42.8 ± 36.6
240 ± 1	6.92	2.84 ± 0.48	75.4 ± 12.8	2.83 ± 0.61	73.8 ± 15.4	139.1 ± 81.4
230 ± 1	5.00	3.30 ± 0.38	212 ± 12	3.30 ± 3.96	193 ± 99	1309 ± 480
220 ± 1	2.30	3.80 ± 0.64	480 ± 42	3.81 ± 5.38	475 ± 270	3659 ± 1410

[a]Uncertainties are 2σ.

temperatures for R2b/R2 result from the onset of the temperature dependence of either of the other two channels. It is also possible that our experiments are not able to effectively constrain the parameters of the fit, and the secondary distributions observed at lower temperatures are the result of increased uncertainties in the rate coefficients in the kinetic mechanism at lower temperatures. A temperature dependence study monitoring the direct products of R2 (the accretion product, the alkoxy product, or the acetonoxy radical), such as an extension of the work by Berndt et al.,[27] would be necessary to both confirm the correct product distributions and to report the branching fractions for each channel. However, as the distributions with the higher values for R2b/R2 follow the temperature trend observed at higher temperatures (T = 296−330 K), we believe the values we reported in Table 2 to be the correct observation of the alkoxy channel pathway.

https://doi.org/10.1021/acs.jpca.3c03660
J. Phys. Chem. A 2023, 127, 7772−7792

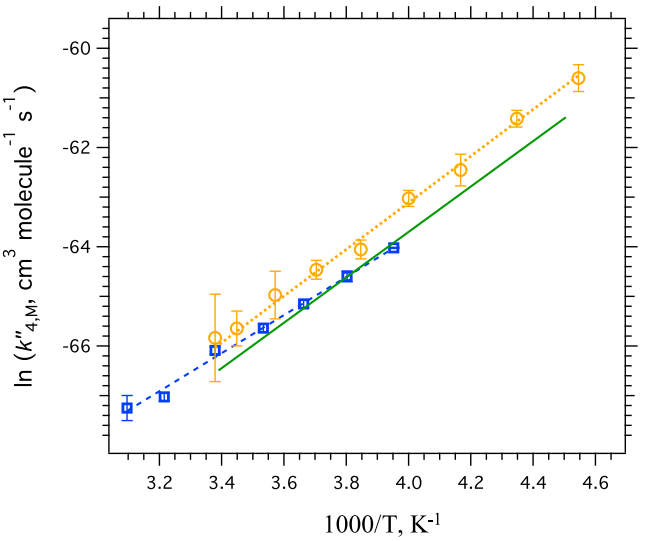

Figure 12. Arrhenius plots of the CH_3OH rate enhancement term ($k''_{4,M}$) from this work (yellow circles) and from Tang et al.[36] (blue squares, 30 Torr in N_2). The yellow line is a weighted linear fit of our data points. The blue dashed line is the overall expression from Tang et al.,[36] and the green solid line is the expression from Christensen et al.[35] Each linear expression is shown over the respective temperature ranges that were studied.

In contrast to R2 where two of the three species that we measured were from secondary chemistry, measurements of R1 were constrained by monitoring both reactants and the OH product. The difference in the potential energy surfaces for these two reaction pathways[20] and the results of this work affirm that R1a and R1b should be treated as two separate reactions. Temperature dependence for the hydroperoxide product reaction (R1a) was not observed over the T = 270−330 K temperature range and a large inverse temperature dependence was observed for the OH product reaction (R1b). Over this range of temperatures, the kinetic rate coefficient for the OH pathways, k_{1b}, increased by an order of magnitude.

4.2. Adduct Chaperone Enhancement of the HO_2 Self-Reaction. *4.2.1. Temperature Dependence HO_2·CH_3OH Equilibrium Constant.* The thermodynamic parameters for the H-bonding reaction forming the HO_2·CH_3OH complex determined in this work are compared to those reported by previous studies for this and similar adducts in Table 7. The results from this work are consistent with both the experimental values and the ab initio calculation reported by Christensen et al.[35] Compared to their work, our values were determined with increased precision and over a larger temperature range (T = 220−280 K compared to T = 231−261 K). Based on the agreement between our experimental result for $\Delta_r S^\circ_T$ and the statistical mechanical result from the ab initio calculations,[35] the calculated value of −106 J mol^{-1} K^{-1} for a fixed value of $\Delta_r S^\circ_T$ was used to calculate a third-law value of $\Delta_r H^\circ_T$ = −37.5 ± 0.25 kJ mol^{-1} in this work. We believe this to be the most accurate value for this parameter.

Bloss et al.[54] measured the equilibrium constant of HO_2·CH_3OH formation at room temperature, reporting $K_{c,M}$ = (6.1 ± 0.9) × 10^{-19} cm^3 molecule^{-1}, uncertainty assumed to be 2σ. Using the reaction thermodynamics results from this work, we estimate $K_{c,M}$ (298 K) = (4.0 ± 1.1) × 10^{-19} cm^3 molecule^{-1}, which is in good agreement, especially given the extrapolation to room temperature where the equilibrium constant is very small. For the smaller value of $\Delta_r H^\circ_T$ reported by Andersson et al.[37] at room temperature, listed in Table 7, a very different value of $\Delta_r S^\circ_T$ of between 60 and 65 J mol^{-1} K^{-1}, compared to the calculated value, would be required, to obtain this room temperature $K_{c,M}$.

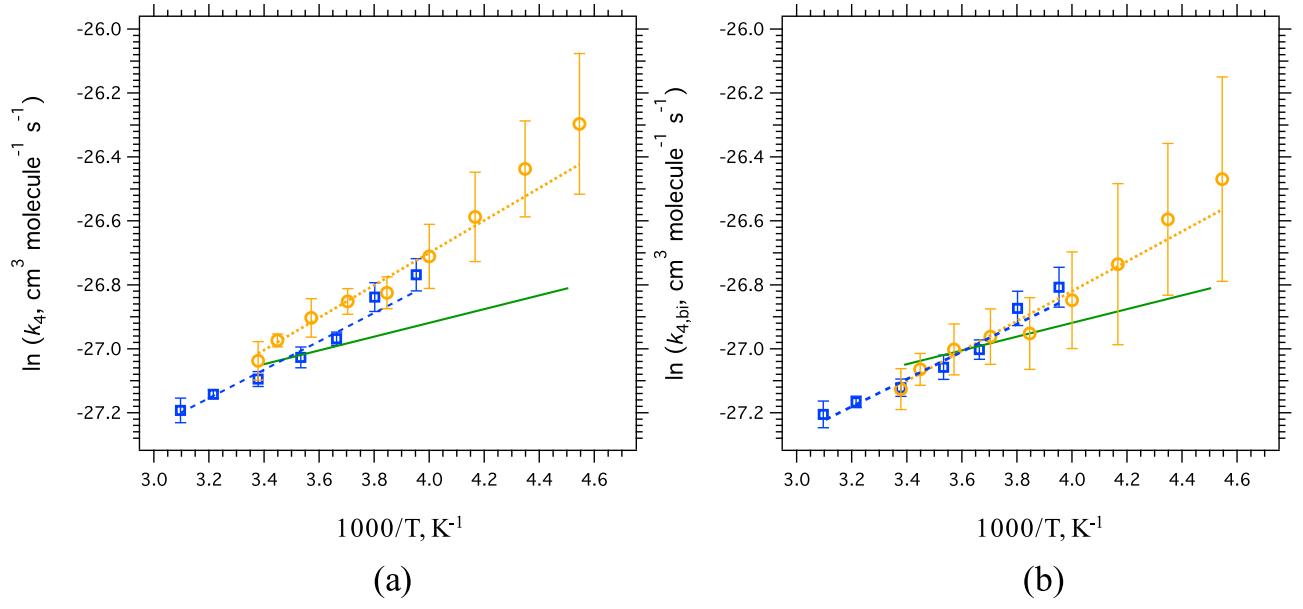

Figure 13. (a) Weighted (variance^{-1}) Arrhenius plot of the HO_2 self-reaction rate coefficient, k_4, in the limit of [CH_3OH] = 0 (k_4) at 100 Torr. Data points (yellow circles) and fit (yellow line) from this work are compared to the values from Christensen et al.[35] (green line) and Tang et al.[36] (blue squares, blue line). Each expression is shown over the respective temperature ranges that were studied. (b) Weighted (variance^{-1}) Arrhenius plot of the HO_2 bimolecular self-reaction rate coefficient, $k_{4,bi}$, demonstrating the excellent agreement between our work (data points, yellow circles; fit, yellow line) and Tang et al.[36] (blue squares and blue dashed line). Each expression is shown over the respective temperature ranges that were studied. Error bars include uncertainty in measured k_4 and calculated $k_{4,ter}$ (as given in JPL 19-5[35]) as the square root of sum squares.

https://doi.org/10.1021/acs.jpca.3c03660
J. Phys. Chem. A 2023, 127, 7772−7792

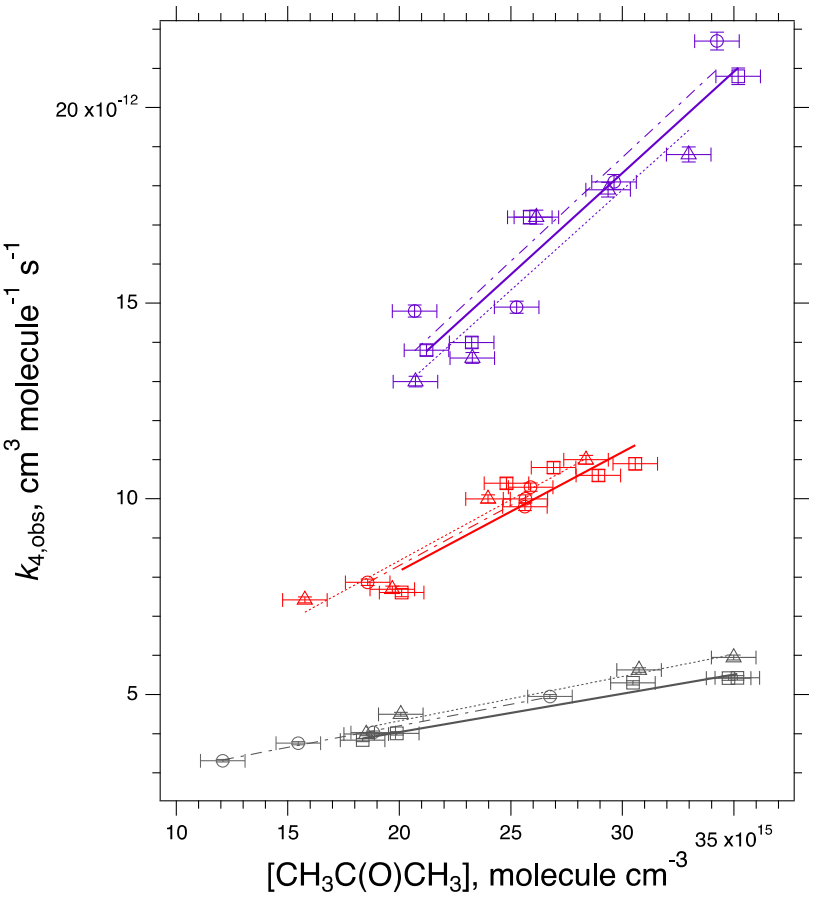

Figure 14. Observed HO_2 self-reaction rate coefficient, $k_{4,obs}$, as a function of $[CH_3C(O)CH_3]_0$ for T = 290 ± 1 K (gray), 280 ± 1 K (red), and 270 ± 1 K (purple). Linear regression fits are shown for each average $[CH_3OH]_0$ used (molecule cm^{-3}): (4.22 ± 0.01) × 10^{15} (gray, circles, dot-dashed line), (5.82 ± 0.02) × 10^{15} (gray, triangles, dotted line), (6.50 ± 0.08) × 10^{15} (gray, squares, bold line), (4.48 ± 0.03) × 10^{15} (red, circles, dot-dashed line), (4.15 ± 0.02) × 10^{15} (red, triangles, dotted line), (6.62 ± 0.01) × 10^{15} (red, squares, bold line), (4.45 ± 0.07) × 10^{15} (purple, circles, dot-dashed), (3.45 ± 0.03) × 10^{15} (purple, triangles, dotted line), and (5.22 ± 0.02) × 10^{15} (purple, squares, bold line).

Table 6. $k''_{4,A}$ from the Linear Regression Fits in Figure 13 with 2σ Uncertainties and the Calculated $k_{4,M} = k_4 + k''_{4,M}[CH_3OH]$ Derived from the Results in Section 3.3.2 for Each Temperature

T, K	$[CH_3OH]$, 10^{-15} molecule cm^{-3}	$k''_{4,A}$ 10^{29} cm^6 $molecule^{-2}$ s^{-1}	intercept 10^{12} cm^3 $molecule^{-1}$ s^{-1}	$k_{4,M}$ (calc.) 10^{12} cm^3 $molecule^{-1}$ s^{-1}
289.9 ± 1	4.22 ± 0.01	11.0 ± 0.96	2.00 ± 0.18	2.06
290.1 ± 1	5.82 ± 0.02	11.3 ± 2.7	2.06 ± 0.72	2.11
290.1 ± 1	6.50 ± 0.08	9.79 ± 1.9	2.09 ± 0.54	2.14
280.8 ± 1	4.48 ± 0.03	30.7 ± 7.3	2.16 ± 1.76	2.17
280.6 ± 1	4.15 ± 0.02	31.1 ± 11.7	2.20 ± 2.64	2.15
279.7 ± 1	6.62 ± 0.01	30.4 ± 17.6	2.08 ± 4.66	2.17
270.3 ± 1	4.45 ± 0.07	53.0 ± 26	2.82 ± 7.28	2.62
269.7 ± 1	3.45 ± 0.03	51.3 ± 20.2	2.51 ± 5.42	2.29
270.2 ± 1	5.22 ± 0.02	51.8 ± 17.7	2.78 ± 4.76	2.47

Compared to the other HO_2 H-bonded adducts listed in Table 7, where the bonding is with an oxygen atom, our thermodynamic parameters for $HO_2{\cdot}CH_3OH$ are similar to those for the $HO_2{\cdot}H_2O$ and $HO_2{\cdot}CH_3C(O)CH_3$ complexes. This similarity is not the case for the $HO_2{\cdot}NH_3$ complex, the work by Hamilton and Lii,[53] where the H-bond is formed with the nitrogen atom.

4.2.2. HO_2 Self-Reaction Methanol Enhancement Term, $k''_{4,M}$. The Arrhenius parameters for $k''_{4,M}$ determined in Section 3.3.2 as well as the parameters determined by Tang et al.[36] and Christensen et al.[34] are given in Table 8. Direct comparison of k''_4 with Christensen et al. (that monitored HO_2 decay using UV absorption) is somewhat limited because the NIR absorption (used in our work and that of Tang et al.) and UV inherently observe different decay rates. The UV measures absorbance by both HO_2 and $HO_2{\cdot}CH_3OH$ (assumed to have the same UV absorption cross section), whereas the NIR measurement, being a discrete rotational line, only measures HO_2 absorbance. As a result, the NIR and UV probes observe different rate constants at lower temperatures due to the presence of the complex. For the UV kinetics at sufficiently low $[CH_3OH]$ ($K_{c,M}[CH_3OH] \ll 1$), it is shown[34,47] that

$$k_{4,obs,M(UV)} = k_4 + (k_{12} - 2k_4)K_{c,M}[CH_3OH] \quad \text{(E13)}$$

https://doi.org/10.1021/acs.jpca.3c03660
J. Phys. Chem. A 2023, 127, 7772−7792

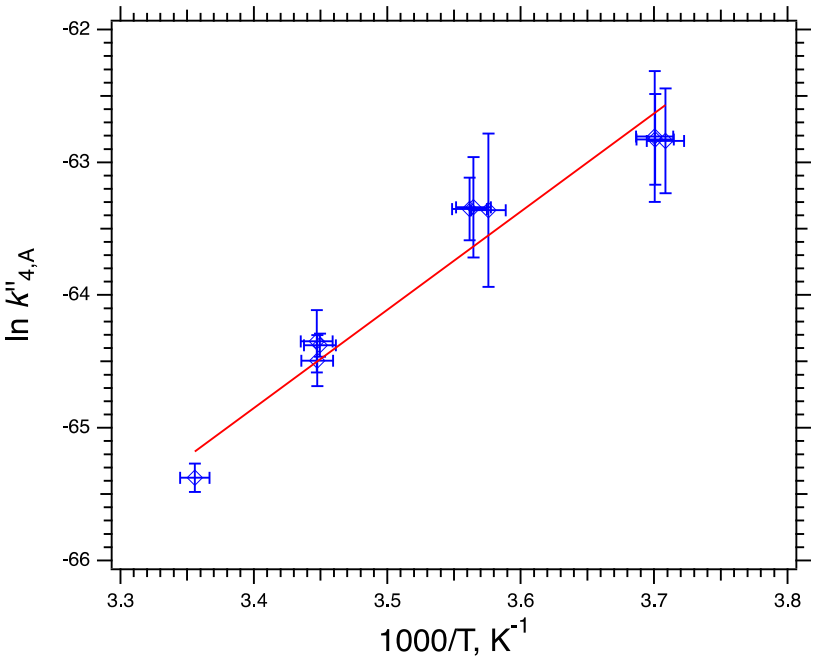

Figure 15. Arrhenius plot of the $CH_3C(O)CH_3$ rate enhancement term, $k''_{4,A}$, shown with the weighted (by σ^{-1}) linear fit (red line) to the data points (blue diamonds) with 2σ error bars. The fit results are $\ln A''_{4,A} = -90.0 \pm 4.1$; $E_a/R = -7396 \pm 1172$ K ($R^2 = 0.952$). The data point at $1000/T = 3.356$ ($T = 298$ K) is from Zuraski et al.[18]

Table 7. Comparison of Thermodynamic Parameters for Several H-Bond Complexes Containing HO_2

complex	$\Delta_r H_T°$ (kJ mol^{-1})	$\Delta_r S_T°$ (J mol^{-1} K^{-1})	references	method[a]
$HO_2{\cdot}CH_3OH$	−38.6 ± 3.3	−110 ± 13	this work (2nd Law)	NIR WMS
	−37.5 ± 0.25	−106[b]	this work (3rd Law)	
	−37.4 ± 9.6	−100 ± 38	Christensen et al[35]	NIR WMS
	−25 ± 3		Andersson et al[37]	UVA
	−36.8	−106	Christensen et al.[35]	CCSD(T)/6-311++G(3df,3pd)
$HO_2{\cdot}H_2O$	−36 ± 16	−85 ± 40	Aloisio et al[47]	FT-IR
	−31 ± 4	−83 ± 14	Kanno et al.[48,49]	NIR-TTFMS
	−32	−107	Aloisio and Francisco[50]	CCSD(T)/6-311++G(2df,2p)
	−31	−103	Hamilton and Naleway[51]	HF/G(3s 1p/1s)
	−21.4		Lendvay[52]	QCISD(T)/6-311++G(2d,2p)
$HO_2{\cdot}CH_3C(O)CH_3$	−35.4 ± 4.0	−88.2 ± 17	Grieman et al[38]	NIR WMS
$HO_2{\cdot}NH_3$	−54 ± 6.3	−140 ± 21	Hamilton and Lii[53]	EPR

[a]NIR WMS = near-IR wavelength-modulation spectroscopy; UVA = ultraviolet absorption; FT-IR = Fourier transform IR spectroscopy; NIR-TTFMS = near-IR continuous-wave two-tone frequency modulation absorption spectroscopy; EPR = electron pulse radiolysis. [b]Calculated value[34] held fixed. Uncertainties are 2σ.

Table 8. Arrhenius Parameters for $k''_{4,M}$ and $k''_{4,A}$. Uncertainties Are 2σ.

T(K), P(Torr)	$A''_{4,M}$ (10^{35} cm^6 s^{-1})	$E''_{4,M}/R$ (K)	$A''_{4,A}$ (10^{40} cm^6 s^{-1})	$E''_{4,A}/R$ (K)	references
220−296, 100	$0.27^{+0.47}_{-0.17}$	−4700 ± 255			this work
253−323, 30	3.9 ± 3.74	−3849 ± 270			Tang et al.[37]
231−261, 100	$0.25^{+0.59}_{-0.11}$	−4570 ± 240			[a]Christensen et al.[34]
270−298, 100			$8.36^{+492}_{-8.22}$	−7396 ± 1172	this work

[a]$k''_{4,M}$ was determined via UVA which leads to a slightly smaller value of $k''_{4,M}$ than measured via NIR in this work and in Tang et al. See text.

$$k''_{4,M(UV)} \equiv (k_{12} - 2k_4)K_{c,M} \quad \text{(E14)}$$

Because the total amount of HO_2 radicals (complexed and non-complexed) is not observed in the NIR, the NIR probe observes a faster apparent decay rate, as given by E12, $k''_{4,M(IR)} = (k_{12} - k_4)K_{c,M}$. However, as shown below (Section 4.2.4) and in previous studies,[35,54] k_{12} is an order of magnitude larger than k_4 which then only results in a decrease of ∼10%.

Comparing the $k''_{4,M}$ Arrhenius parameters given in Table 8 and the associated plots in Figure 12, significant differences are found between Tang et al. and Christensen et al., which was part of the motivation for the re-examination of the methanol chaperone effect on the HO_2 self-reaction. Our values of both the pre-exponential factor, $A''_{4,M}$, and the activation energy parameter, $E''_{4,M}/R$, are found to agree with Christensen et al.[35] As expected, we systematically obtained slightly higher values

https://doi.org/10.1021/acs.jpca.3c03660
J. Phys. Chem. A 2023, 127, 7772−7792

Table 9. Comparison of Arrhenius Parameters for k_4 and $k_{4,bi}$. Uncertainties Are 2σ

T(K), P(Torr)	A_4 (10^{13} cm^3 s^{-1})	E_4/R (K)	$A_{4,bi}$ (10^{13} cm^3 s^{-1})	$E_{4,bi}/R$ (K)	references
220−296, 100	$3.34^{+1.04}_{-0.80}$	−507 ± 76	$3.47^{+1.19}_{-0.88}$ [a]	−468 ± 82[a]	this work
253−323, 30	3.95 ± 0.50	−439 ± 78	$3.97^{+1.20}_{-0.92}$ [a]	−430 ± 78[a]	Tang et al.[36]
222−295, 100	8.8 ± 0.9	−210 ± 26	15 ± 2[a]	−28 ± 31[a]	Christensen et al.[34]
252−391, 1−7			2.0 ± 0.6	−595 ± 120	Takacs and Howard[55]
298−358, 7−20			2.4[b]	−560 ± 200	Thrush and Tyndall[56]
230−420, 100−700			2.2 ± 0.5	−620 ± 60	Kircher and Sander[57]
222−1120	2.6	−533	3.0	−460	JPL 19-5[42]

[a] $k_{4,bi}$ parameters determined here from k_4 using $k_{4,ter}$ from JPL 19-5. [b] No uncertainty given.

of $k''_{4,M}$ over the overlapping temperature range due to IR detection of the decay rate compared to UVA detection as explained above. Agreement is also found between all three of these studies for the value of $A''_{4,M}$, but the uncertainty in this parameter is large. Figure 12 shows agreement between the measured $k''_{4,M}$ values from Tang et al., but the values for the slope are not in agreement. The Arrhenius equation for the analogous enhancement coefficient for the HO_2 self-reaction caused by the complex formed with water,[36] where A''_{H_2O} = $(1.16 \pm 0.58) \times 10^{-36}$ cm^6 s^{-1} and = E''_{H_2O}/R = (4614 ± 145) K which are very similar to our values for the methanol case; this similarity may support our findings given the similar H-bond in the two complexes and size of the molecule bonded to HO_2.

4.2.3. HO_2 Self-Reaction Rate Constant, k_4. The Arrhenius parameters for k_4 derived here are listed in Table 9 along with those from other studies for comparison. Although the experiments were performed at different pressures, the values for k_4 in Table 9 are still comparable because there is only a 10% increase related to the pressure between 0 and 100 Torr. To remove this point of possible confusion, the $k_{4,bi}$ parameters calculated from our results and those of Tang et al. are also provided in Table 9. One notable difference seen in the table is the better precision of A_4 for Tang et al. When an inverse-variance weighted fit is carried out on the data provided in their paper is performed, as we did for our data, we obtain A_4 = $(3.91^{+1.10}_{-0.86}) \times 10^{-13}$ cm^3 molecule^{-1} s^{-1} and E_4/R = −442 ± 73 K, which is more in line with our uncertainties for similar data.

Regardless, our results are in very good agreement with the JPL 19-5 recommendations[42] and in excellent agreement with those of Tang et al.[36] This excellent agreement is particularly true for $k_{4,bi}$, especially in the overlapping temperature regions. This agreement is made clear pictorially in Figure 13b where weighted fits of both sets of data in an Arrhenius plot are depicted. In fact, from their respective Arrhenius expressions, both studies result in a $k_{4,bi}$ (298 K) of 1.7×10^{-12} cm^3 molecule^{-1} s^{-1} rather than the 1.4×10^{-12} cm^3 molecule^{-1} s^{-1} given in the JPL 19-5 recommendation.[42] This difference from the recommended value is further confirmed by the direct measurement in both studies at T = 296 K of $k_{4,bi}$, yielding 1.66×10^{-12} cm^3 molecule^{-1} s^{-1} with a 2σ uncertainty of ±0.11 and ±0.04 cm^3 molecule^{-1} s^{-1} in our work and Tang et al.,[36] respectively.

In considering comparison with the older studies, it should be noted that only the works by Christensen et al.[34] and Tang et al.[36] accounted for the CH_3OH chaperone effect in their analysis. Agreement with the older studies is then reasonable. As Tang et al. have noted, the results of Christensen et al.[34] showing a very weak temperature dependence for k_4 and, especially, for $k_{4,bi}$, do not agree with the results of the other studies including ours (Note that we have corrected Christensen et al.'s results for the latest recommendation for $k_{4,ter}$.). No explanation for this difference could be determined.

4.2.4. Temperature Dependence of the HO_2 Self-Reaction Acetone Enhancement Term, $k''_{4,A}$. Because this is the first determination of the temperature dependence of the chaperone enhancement term for the HO_2 self-reaction due to acetone, $k''_{4,A}$, no comparisons with other studies are included in Table 8. At room temperature, acetone was shown to have a much greater chaperone effect on the HO_2 self-reaction than that of methanol due to a combination of a larger equilibrium constant for hydrogen-bonded complex formation ($K_{C,A} > K_{C,M}$) with a larger chaperone enhancement term ($k''_{4,A} > k''_{4,M}$).[17] As the temperature is decreased below room temperature, the relative magnitude of the chaperone effect due to the acetone H-bonded complex compared to that formed from methanol can be determined from the respective complex formation equilibrium thermodynamic parameters given in Table 7 and the Arrhenius parameters given for the respective chaperone enhancement coefficients found in Table 8. Whereas the negative activation energy parameters differ by greater than a factor of 1.5, the thermodynamic parameters are very similar. In fact, the larger increase in the chaperone effect with decreasing temperature found for acetone compared to methanol is due almost solely to k''_4. For example, using the respective Arrhenius equations for the chaperone enhancement coefficients, the ratio of $k''_{4,A}/k''_{4,M}$ increases by a factor of 2.6 in going from T = 298 K to T = 270 K, whereas the equilibrium constant ratio, $K_{C,A}/K_{C,M}$, remains approximately the same. Clearly, the acetone chaperone effect must be accounted for in laboratory studies of radical reactions of HO_2 when acetone is present at any appreciable concentration over a wide temperature range including and above room temperature.

4.2.5. Determination of Rate Coefficients for Chaperone Reactions of HO_2 with Hydrogen-Bonded Complexes for Both Methanol and Acetone. Using the temperature dependence of k''_4 and k_4 for CH_3OH and $CH_3C(O)CH_3$ combined with the temperature dependence of the respective equilibrium constants, $K_{c,M}$ and $K_{c,A}$, estimates for the rate coefficients for the chaperone enhancement reaction for both species can be determined, respectively, R12 for CH_3OH and R15 for $CH_3C(O)CH_3$

$$k_{12} = \frac{k''_{4,M}}{K_{C,M}} + k_4 \quad \text{(E15)}$$

$$k_{15} = \frac{k''_{4,A}}{K_{C,A}} + k_4 \quad \text{(E16)}$$

For CH_3OH, using our data values for $k''_{4,M}$ and k_4 from Table 5 and $K_{c,M}$ from Table 4, over the temperature range of

https://doi.org/10.1021/acs.jpca.3c03660
J. Phys. Chem. A 2023, 127, 7772−7792

Table 10. Rate Coefficients for the Chaperone Reaction $HO_2 + HO_2{\cdot}X \rightarrow H_2O_2 + O_2 + X$ for X = CH_3OH (k_{12}) and X = $CH_3C(O)CH_3$ (k_{15})[a]

T (K)	k_{12} 10^{11} cm^3 molecule^{-1} s^{-1} from data	k_{12} 10^{11} cm^3 molecule^{-1} s^{-1} from equations	k_{15} 10^{11} cm^3 molecule^{-1} s^{-1} from equations
298			3.58
290			5.10
280	6.94 ± 2.2	5.26	8.23
270	6.53 ± 1.9	5.50	13.8
260	4.11 ± 0.33	5.76	
250	5.40 ± 0.51	6.05	
240	4.97 ± 0.80	6.37	
230	7.59 ± 0.50	6.73	
220	7.83 ± 0.68	7.13	

[a]Note: The first column is k_{12} determined directly from data points using E15, whereas the second column is k_{12} calculated from Arrhenius and van't Hoff equations determined in this work for the constants in E15. The third column is k_{15} calculated from E16 from Arrhenius equations determined in this work for the rate coefficients and from the van't Hoff equation for $K_{c,A}$ from JPL 19-5.[42]

220−280 K, the k_{12} values determined are found in column 1 of Table 10 with propagated 2σ uncertainties. An Arrhenius plot of these results, given in Figure 16, yielded a very poor fit

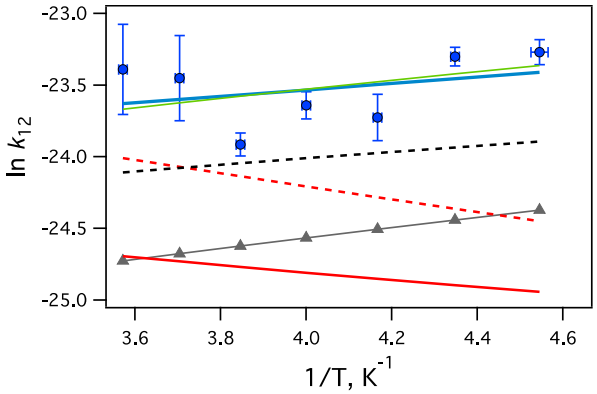

Figure 16. Arrhenius plot of methanol chaperone reaction R12 showing lack of temperature dependence. (Blue circles) Data points (shown with 2σ error bars) calculated via E15 for T = 280−220 K. (Blue line) A linear fit with E_a/R = −224 K and A = 2.6 × 10^{-11} cm^3 molecule^{-1} s^{-1}, R^2 = 0.107; weighted average k_{12} = (5.85 ± 0.25) × 10^{-11} cm^3 molecule^{-1} s^{-1}. (Green line) k_{12} derived from Arrhenius equations and $K_{C,M}$ determined in this work for constants in E15, yielding E_a/R = −314 K and A = 1.72 × 10^{-11} cm^3 molecule^{-1} s^{-1}. Comparison with k_{12} calculated from results in Tang et al.[36] (red) and in Christensen et al.[34] (black) using (solid lines) $K_{c,M}$ from Christensen et al. (solid lines) and using $K_{c,M}$ from this work (dashed lines).

(R^2 = 0.11) that suggests no temperature dependence for k_{12}. A weighted average (using inverse-variance) yielded (with 2σ uncertainty) k_{12} = (5.85 ± 0.25) × 10^{-11} cm^3 molecule^{-1} s^{-1}. This chaperone reaction rate coefficient is a factor of approximately 20 greater than the rate coefficient for the HO_2 self-reaction, k_4, demonstrating the impact of this effect on the HO_2 self-reaction rate under these laboratory conditions.

An Arrhenius expression for k_{12} can also be determined using the temperature-dependent equations derived in this work for $k''_{4,M}$, k_4, and $K_{c,M}$

$$k_{12} = (1.72 \pm 0.050 \times 10^{-11}) \exp[(314 \pm 7.2)/T] \text{ cm}^3 \text{ molecule}^{-1} \text{ s}^{-1} \quad \text{(E17)}$$

which further exhibits weak temperature dependence, with an activation energy of only 2.6 kJ mol^{-1}. Values for k_{12} calculated from E17 at the experimental temperatures used are given in column 2 of Table 10 and an Arrhenius plot of E17 is also shown in Figure 16. The derived Arrhenius equation is observed to fit the data points very well, although the scatter in the data does not warrant a claim of determined temperature dependence for k_{12}. Over this temperature range, E17 yields a slightly higher value of $k_{12} \approx 6 \times 10^{-11}$ cm^3 molecule^{-1} s^{-1}. However, the propagation of error from the three equations for the parameters used to determine k_{12} in this manner yields an exceptionally large uncertainty.

Lastly, plotted in Figure 16 is a comparison between our results with those of Tang et al.[36] (who measured only HO_2 decay in the IR) extrapolated to lower temperatures than they measured (T < 253 K) and Christensen et al.[34] (who measured combined HO_2 and $HO_2{\cdot}CH_3OH$ decay in UV) derived from their determinations of $k''_{4,M}$ and $K_{c,M}$. (We converted $k''_{4,M}$ (UV) in Christensen et al. to $k''_{4,M}$ (IR) for this comparison.) Given that our $K_{c,M}$ is smaller than that of Christensen et al. and our $k''_{4,M}$ is larger than that of both their work and that of Tang et al., it is not surprising that our value of k_{12} is larger than that we derived from the equations determined in their works, k_{12} = 2.0 × 10^{-11} and 1.7 × 10^{-11} cm^3 molecule^{-1} s^{-1}, respectively. However, Tang et al. used Christensen et al.'s value for $K_{C,M}$. If the $K_{C,M}$ determined here is used instead, Tang et al.'s value becomes k_{12} = 3.3 × 10^{-11}, and similarly, Christensen et al.'s value is k_{12} = 3.6 × 10^{-11} cm^3 molecule^{-1} s^{-1}, both in better agreement with our value. It also more clearly shows the difference in k_{12} stemming from the different values found for $k''_{4,M}$ here compared to these other studies. (The magnitude of k_4 is much smaller than that of the ratio $k''_{4,M}$ and $K_{c,M}$ so is of little consequence). Note again that the propagated uncertainties using derived equations are very large and not given here. The other direct determinations of k_{12} are from Christensen et al.[34,35] where they found k_{12} = (2.1 ± 0.7) × 10^{-11} cm^3 molecule^{-1} s^{-1} for T = 231−261 K and Bloss et al.[54] who measured k_{12} = (3.2 ± 0.5) × 10^{-11} cm^3 molecule^{-1} s^{-1} for T = 298 K and P = 760 Torr.

For acetone, the temperature dependence of the chaperone effect was measured and is presented here for the first time. Because we did not remeasure the equilibrium constant for the formation of the complex, R14, the reaction coefficient for the acetone chaperone reaction, R15, can only be determined from the combined Arrhenius equations for k_4 and $k''_{4,A}$ derived in

https://doi.org/10.1021/acs.jpca.3c03660
J. Phys. Chem. A 2023, 127, 7772−7792

Table 11. Rate Coefficients, k_{13}, for the $HO_2{\cdot}CH_3OH$ Self-Reaction Determined from k_4'' and k_4''' Found from Polynomial Fits of the Nonlinear Curves of $k_{4,obs}$ vs $[CH_3OH]$ at the Four Lowest T Studied[a]

T(K)	$K_{C,M}$ (data) 10^{18} molecule cm^{-3}	k_{13} (data) 10^{11} cm^3 molecule^{-1} s^{-1}	$K_{C,M}$ (vH) 10^{18} molecule cm^{-3}	k_{13} (from vH) 10^{11} cm^3 molecule^{-1} s^{-1}
250	8.3 ± 0.70	10.7 ± 5.4	6.7	14.90
240	16.1 ± 0.30	10.0 ± 3.3	14.0	12.40
230	29.2 ± 1.1	22.0 ± 6.6	31.1	19.70
220	64.4 ± 1.7	16.2 ± 5.4	74.5	13.00

[a]Uncertainties are 2σ. (vH = van't Hoff; see text.)

this work and the equilibrium constant $K_{c,M}$ from JPL-15,[37] yielding

$$k_{15} = [(7.9 \pm 0.72) \times 10^{-17}]\exp[(3881 \pm 25)/T] \text{ cm}^3 \text{ molecule}^{-1} \text{ s}^{-1} \quad \text{(E18)}$$

Values calculated for k_{15} using E18 at the experimental temperatures used in this study are given in column three of Table 10. Albeit over different temperature ranges, the resulting rate coefficient for the acetone chaperone enhancement is observed to be larger than that due to methanol and to have a significant temperature dependence compared to a very slight temperature dependence for methanol, E17.

Finally, with respect to chaperone effects, the curvature found for $k_{4,obs}$ as a function of $[CH_3OH]$ when $T \leq 250$ K can be fit via the quadratic equation, E9, to determine the k_4'' and k_4''' coefficients which in turn allows the calculation of the reaction coefficient for the reaction between two hydrogen-bonded complex molecules, R13

$$k_{13} = \frac{k_4'''}{K_{C,M}^2} + k_{12} - k_4 = \frac{k_4'''}{K_{C,M}^2} + \frac{k_4''}{K_{C,M}} \quad \text{(E19)}$$

using E15. From the polynomial fits of $k_{4,obs}$ vs $[CH_3OH]$ for T = 220−250 K shown in Figure 11a, the values determined for k_4'' and k_4''' are given in Table 5 along with their 2σ uncertainties. Combining these values with the $K_{c,M}$ (with their uncertainties), the k_{13} rate coefficients at these four temperatures are given in Table 11. For comparison, the k_{13} rate coefficients were also calculated using the van't Hoff equation determined in this work for $K_{c,M}$, both of which are given in the last two columns of Table 11. With apparently no temperature dependence, a weighted average of the data-determined values yields a rate coefficient of

$$k_{13} = (1.3 \pm 0.45) \times 10^{-10} \text{ cm}^3 \text{ molecule}^{-1} \text{ s}^{-1} \quad \text{(E20)}$$

The magnitudes of the k_{13} values are seen to be larger than those of k_{12} by approximately a factor of 2. The reaction of two complexes to form the products of the HO_2 self-reaction is then extremely fast despite the complexity of the molecular structure.

The assumption made here is that the increase in rate observed as the temperature decreases is due solely to the reactions involving the hydrogen-bonded complexes with one methanol or acetone molecule because of their increased concentration and the increasingly large rate coefficients for the effective self-reaction via the H-bonded complexes. Another possibility that is ignored is the formation of larger complexes that may also increase the apparent HO_2 self-reaction rate due to their reaction with HO_2 and other complexes formed.

5. CONCLUSIONS

This work reports the temperature-dependent rate parameters and branching fractions for the reactions: $CH_3C(O)CH_2O_2$ + HO_2 (R1) and $CH_3C(O)CH_2O_2$ + $CH_3C(O)CH_2O_2$ (R2). This is the first temperature-dependent kinetic study on these reactions. The results for the temperature dependence on the rate coefficients for R1, and specifically the OH production pathway, are important to help resolve discrepancies between atmospheric models and OH field measurements. The results from R2 will aid future laboratory studies involving this class of reactions.

Because of its importance in the overall mechanism of the radical reactions studied here, the temperature dependence of the HO_2 self-reaction (R4) rate coefficient was also re-investigated at 100 Torr over the temperature range T = 220−296 K. The Arrhenius parameters determined for the bimolecular rate constant $k_{4,bi}$ were found to be in good agreement with the JPL 19-5-recommended values but were in excellent agreement with those values measured by Tang et al.[35] (T = 253−323 K), establishing their validity by two different experimental methods over a significant temperature range.

The chaperone enhancement of the HO_2 self-reaction caused by the hydrogen-bonded complexes formed between HO_2 and precursor oxygenated molecules was re-investigated for methanol over our temperature range and studied for acetone for the first time. First, the equilibrium constants of the reaction of HO_2 with CH_3OH to form $HO_2{\cdot}CH_3OH$ were measured at 100 Torr in N_2 from T = 220−280 K from which the enthalpy and entropy of this reaction were determined over this larger temperature range and with better precision than those of previous studies. Agreement with the calculation led to our determination of a precise value for the enthalpy of formation of $HO_2{\cdot}CH_3OH$.

Second, the Arrhenius temperature dependence of the rate enhancement term for the HO_2 self-reaction rate constant (which adds to the bimolecular rate constant proportionally with $[CH_3OH]$) was determined and found to agree with a previous measurement performed over a smaller temperature range. At higher $[CH_3OH]$ and lower temperatures, a second nonlinear rate enhancement term (adding proportionally with $[CH_3OH]^2$) was able to be measured for the first time with no discernible temperature dependence detected.

Coupling these enhancement terms with the equilibrium constant and the bimolecular HO_2 self-reaction rate constant, the bimolecular rate constants for the other reactions in the chaperone mechanism (R12 and R13) were calculated and both were found to have a very weak temperature dependence. More interestingly, the rate coefficients for HO_2 + $HO_2{\cdot}CH_3OH$ (R12) and for $HO_2{\cdot}CH_3OH$ + $HO_2{\cdot}CH_3OH$ (R13) were found to be successively significantly greater than the self-reaction itself in forming the H_2O_2 + O_2 products. For example, at T = 240 K, the rate coefficients increase as 2.4 ×

https://doi.org/10.1021/acs.jpca.3c03660
J. Phys. Chem. A 2023, 127, 7772−7792

10^{-12}, 6.4×10^{-11}, and 1.3×10^{-10} cm^3 $molecule^{-1}$ s^{-1} for R4, R12, and R13, respectively.

Similar experiments and analyses were performed to discover the chaperone enhancement for the acetone case for the temperature range T = 270−298 K. Unlike the methanol case, the increased rate of the HO_2 self-reaction due to the $HO_2{\cdot}CH_3C(O)CH_3$ adduct is easily observable even at room temperature because of the larger equilibrium constant for forming the hydrogen-bonded complex from HO_2 and $CH_3C(O)CH_3$. The analogous rate enhancement term for the HO_2 self-reaction rate constant (which adds to the bimolecular rate constant proportionally with $[CH_3C(O)CH_3]$) was determined and found to have a much greater temperature dependence than that for methanol. In fact, the analogous rate constant for the HO_2/hydrogen-bonded complex reaction for acetone (R15) determined from the rate enhancement term and the equilibrium constant is found to have a large Arrhenius temperature dependence with a negative activation energy greater than that of the methanol by more than a factor of 10. In addition, the rate constant for the reaction of HO_2 with the respective hydrogen complex is larger for acetone than it is for methanol, e.g., at T = 270 K, 1.4×10^{-10} and 5.5×10^{-11} cm^3 $molecule^{-1}$ s^{-1} for R15 and R12, respectively. Perhaps, acetone, the larger molecule with more vibrational modes than methanol, is a more effective immediate "collision" partner than methanol for the HO_2 self-reaction mechanism that goes through a H_2O_4* ring transition state. In any case, laboratory studies involving hydroperoxy and acetone must include the chaperone effect on the HO_2 self-reaction rate, even above room temperature.

■ ASSOCIATED CONTENT

Supporting Information

The Supporting Information is available free of charge at https://pubs.acs.org/doi/10.1021/acs.jpca.3c03660.

Response to the 2022 paper by Assali et al.[28] and further discussion of the k_2 MCMC distributions (PDF)

■ AUTHOR INFORMATION

Corresponding Author

Stanley P. Sander − *NASA Jet Propulsion Laboratory, California Institute of Technology, Pasadena, California 91109, United States;* orcid.org/0000-0003-1424-3620; Email: stanley.p.sander@jpl.nasa.gov

Authors

Kristen Zuraski − *NASA Jet Propulsion Laboratory, California Institute of Technology, Pasadena, California 91109, United States;* Present Address: The Cooperative Institute for Research in Environmental Sciences, University of Colorado Boulder; Chemical Sciences Division, NOAA Earth System Research Laboratory, Boulder, Colorado 80305, United States; orcid.org/0000-0003-3149-6611

Fred J. Grieman − *NASA Jet Propulsion Laboratory, California Institute of Technology, Pasadena, California 91109, United States; Seaver Chemistry Laboratory, Pomona College, Claremont, California 91711, United States*

Aileen O. Hui − *Arthur Amos Noyes Laboratory of Chemical Physics, California Institute of Technology, Pasadena, California 91125, United States;* Present Address: The Aerospace Corporation, El Segundo, California 90245, United States

Julia Cowen − *NASA Jet Propulsion Laboratory, California Institute of Technology, Pasadena, California 91109, United States; Seaver Chemistry Laboratory, Pomona College, Claremont, California 91711, United States*

Frank A. F. Winiberg − *NASA Jet Propulsion Laboratory, California Institute of Technology, Pasadena, California 91109, United States*

Carl J. Percival − *NASA Jet Propulsion Laboratory, California Institute of Technology, Pasadena, California 91109, United States;* orcid.org/0000-0003-2525-160X

Mitchio Okumura − *Arthur Amos Noyes Laboratory of Chemical Physics, California Institute of Technology, Pasadena, California 91125, United States;* orcid.org/0000-0001-6874-1137

Complete contact information is available at: https://pubs.acs.org/10.1021/acs.jpca.3c03660

Notes

The authors declare no competing financial interest.

■ ACKNOWLEDGMENTS

This research was carried out by the Jet Propulsion Laboratory, California Institute of Technology, under contract with the National Aeronautics and Space Administration (NASA), supported by the Upper Atmosphere Research and Tropospheric Chemistry Programs. The contribution of K.Z. was supported by the appointment to the NASA Postdoctoral Program at the NASA Jet Propulsion Laboratory, administered by the Universities Space Research Association under contract with NASA. The contribution from A.H. was supported in part by the National Science Foundation (NSF grant no. CHE-1413712) and the NASA Earth and Science Fellowship (NESSF). This research was also supported by an appointment of F.J.G. to the Senior NASA Postdoctoral Program at the Jet Propulsion Laboratory, administered by Oak Ridge Associated Universities through a contract with NASA and a SURP grant from Pomona College for J.A.C.

■ REFERENCES

(1) Schervish, M.; Donahue, N. M. Peroxy radical kinetics and new particle formation. *Environ. Sci. Atmos.* **2021**, *1*, 79−92.

(2) Monks, P. S. Gas-phase radical chemistry in the troposphere. *Chem. Soc. Rev.* **2005**, *34*, 376−395.

(3) Orlando, J. J.; Tyndall, G. S. Laboratory studies of organic peroxy radical chemistry: an overview with emphasis on recent issues of atmospheric significance. *Chem. Soc. Rev.* **2012**, *41*, 6294−6317.

(4) Tyndall, G. S.; Cox, R. A.; Granier, C.; Lesclaux, R.; Moortgat, G. K.; Pilling, M. J.; Ravishankara, A. R.; Wallington, T. J. Atmospheric chemistry of small organic peroxy radicals. *J. Geophys. Res. Atmos.* **2001**, *106*, 12157−12182.

(5) Vereecken, L.; Francisco, J. S. Theoretical studies of atmospheric reaction mechanisms in the troposphere. *Chem. Soc. Rev.* **2012**, *41*, 6259−6293.

(6) Wolfe, G. M.; Cantrell, C.; Kim, S.; Mauldin, R. L., III; Karl, T.; Harley, P.; Turnipseed, A.; Zheng, W.; Flocke, F.; Apel, E. C.; et al. Missing peroxy radical sources within a rural forest canopy. *Atmos. Chem. Phys. Discuss.* **2013**, *13*, 31713−31759.

(7) Kjaergaard, H. G.; Møller, K.; Otkjaer, R. V.; Wennberg, P.; Crounse, J. D.; Xu, L.; Praske, E. J.; Bates, K. H. Atmospheric autoxidation via fast peroxy radical hydrogen shift reactions. In *258th ACS National Meeting and Exposition*; CaltechAUTHORS: San Diego, CA, 2019, pp 25−29.

(8) Crounse, J. D.; Nielsen, L. B.; Jorgensen, S.; Kjaergaard, H. G.; Wennberg, P. O. Autoxidation of Organic Compounds in the Atmosphere. *J. Phys. Chem. Lett.* **2013**, *4*, 3513−3520.
(9) Wennberg, P. O.; Xu, L.; Crouse, J.; Møller, K.; Kjaergaard, H. G. Unimolecular chemistry of organic peroxy radicals in the atmosphere. In *Abstracts of Papers of the American Chemical Society*; CaltechAUTHORS, 2019, p 258.
(10) Møller, K. H.; Bates, K. H.; Kjaergaard, H. G. The Importance of Peroxy Radical Hydrogen-Shift Reactions in Atmospheric Isoprene Oxidation. *J. Phys. Chem. A* **2019**, *123*, 920−932.
(11) Jenkin, M. E.; Valorso, R.; Aumont, B.; Rickard, A. R. Estimation of rate coefficients and branching ratios for reactions of organic peroxy radicals for use in automated mechanism construction. *Atmos. Chem. Phys.* **2019**, *19*, 7691−7717.
(12) Shallcross, D. E.; Teresaraventosduran, M.; Bardwell, M. W.; Bacak, A.; Solman, Z.; Percival, C. J. A semi-empirical correlation for the rate coefficients for cross- and self-reactions of peroxy radicals in the gas phase. *Atmos. Environ.* **2005**, *39*, 763−771.
(13) Daub, C. D.; Valiev, R.; Salo, V.-T.; Zakai, I.; Gerber, B.; Kurtén, T. Computed Pre-reactive complex association lifetimes explain trends in experimental reaction rates for peroxy radical recombinations. *ACS Earth Space Chem.* **2022**, *6*, 2446−2452.
(14) Franco, B.; Clarisse, L.; Stavrakou, T.; Muller, J. F.; Pozzer, A.; Hadji-Lazaro, J.; Hurtmans, D.; Clerbaux, C.; Coheur, P. F. Acetone Atmospheric Distribution Retrieved From Space. *Geophys. Res. Lett.* **2019**, *46*, 2884−2893.
(15) Elias, T.; Szopa, S.; Zahn, A.; Schuck, T.; Brenninkmeijer, C.; Sprung, D.; Slemr, F. Acetone variability in the upper troposphere: analysis of CARIBIC observations and LMDz-INCA chemistry-climate model simulations. *Atmos. Chem. Phys.* **2011**, *11*, 8053−8074.
(16) Fischer, E. V.; Jacob, D. J.; Millet, D. B.; Yantosca, R. M.; Mao, J. The role of the ocean in the global atmospheric budget of acetone. *Geophys. Res. Lett.* **2012**, *39*, L01807.
(17) Khan, M. A. H.; Cooke, M. C.; Utembe, S. R.; Archibald, A. T.; Maxwell, P.; Morris, W. C.; Xiao, P.; Derwent, R. G.; Jenkin, M. E.; Percival, C. J.; et al. A study of global atmospheric budget and distribution of acetone using global atmospheric model STOCHEM-CRI. *Atmos. Environ.* **2015**, *112*, 269−277.
(18) Zuraski, K.; Hui, A. O.; Grieman, F. J.; Darby, E.; Møller, K. H.; Winiberg, F. A. F.; Percival, C. J.; Smarte, M. D.; Okumura, M.; Kjaergaard, H. G.; et al. Acetonyl peroxy and hydro peroxy self- and cross-reactions: Kinetics, Mechanism, and Chaperone Enhancement from the perspective of the hydroxyl radical product. *J. Phys. Chem. A* **2020**, *124*, 8128−8143.
(19) Jenkin, M. E.; Hurley, M. D.; Wallington, T. J. Investigation of the radical product channel of the $CH_3C(O)CH_2O_2$+HO_2 reaction in the gas phase. *Phys. Chem. Chem. Phys.* **2008**, *10*, 4274−4280.
(20) Hasson, A. S.; Kuwata, K. T.; Arroyo, M. C.; Petersen, E. B. Theoretical studies of the reaction of hydroperoxy radicals (HO_2•) with ethyl peroxy ($CH_3CH_2O_2$•), acetyl peroxy ($CH_3C(O)O_2$•) and acetonyl peroxy ($CH_3C(O)CH_2O_2$•) radicals. *J. Photochem. Photobiol., A* **2005**, *176*, 218−230.
(21) Dillon, T. J.; Crowley, J. N. Direct detection of OH formation in the reactions of HO_2 with $CH_3C(O)O_2$ and other substituted peroxy radicals. *Atmos. Chem. Phys.* **2008**, *8*, 4877−4889.
(22) Hasson, A. S.; Tyndall, G. S.; Orlando, J. J. A product yield study of the reaction of HO_2 radicals with ethyl peroxy ($C_2H_5O_2$), acetyl peroxy ($CH_3C(O)O_2$), and acetonyl peroxy ($CH_3C(O)$-CH_2O_2) radicals. *J. Phys. Chem. A* **2004**, *108*, 5979−5989.
(23) Bridier, I.; Veyret, B.; Lesclaux, R.; Jenkin, M. E. Flash-Photolysis Study of the UV Spectrum and Kinetics of Reactions of the Acetonylperoxy Radical. *J. Chem. Soc., Faraday Trans.* **1993**, *89*, 2993−2997.
(24) Hasson, A. S.; Tyndall, G. S.; Orlando, J. J.; Singh, S.; Hernandez, S. Q.; Campbell, S.; Ibarra, Y. Branching Ratios for the Reaction of Selected Carbonyl-Containing Peroxy Radicals with Hydroperoxy Radicals. *J. Phys. Chem. A* **2012**, *116*, 6264−6281.
(25) Cox, R. A.; Munk, J.; Nielsen, O. J.; Pagsberg, P.; Ratajczak, E. Ultraviolet-Absorption Spectra and Kinetics of Acetonyl and Acetonylperoxy Radicals. *Chem. Phys. Lett.* **1990**, *173*, 206−210.
(26) Emricha, M.; Warneck, P. Branching ratio for the self-reaction of acetonyl peroxy radicals. *Z. Naturforsch.* **2003**, *58*, 429−433.
(27) Berndt, T.; Scholz, W.; Mentler, B.; Fischer, L.; Herrmann, H.; Kulmala, M.; Hansel, A. Accretion Product Formation from Self- and Cross-Reactions of RO_2 Radicals in the Atmosphere. *Angew. Chem., Int. Ed.* **2018**, *57*, 3820−3824.
(28) Assali, M.; Fittschen, C. Self-reaction of acetonyl peroxy radicals and their reaction with Cl atoms. *J. Phys. Chem. A* **2022**, *126*, 4585−4597.
(29) Carslaw, N.; Creasey, D. J.; Harrison, D.; Heard, D. E.; Hunter, M. C.; Jacobs, P. J.; Jenkin, M. E.; Lee, J. D.; Lewis, A. C.; Pilling, M. J.; et al. OH and HO_2 radical chemistry in a forested region of north-western Greece. *Atmos. Environ.* **2001**, *35*, 4725−4737.
(30) Lelieveld, J.; Butler, T. M.; Crowley, J. N.; Dillon, T. J.; Fischer, H.; Ganzeveld, L.; Harder, H.; Lawrence, M. G.; Martinez, M.; Taraborrelli, D.; et al. Atmospheric oxidation capacity sustained by a tropical forest. *Nature* **2008**, *452*, 737−740.
(31) Kubistin, D.; Harder, H.; Martinez, M.; Rudolf, M.; Sander, R.; Bozem, H.; Eerdekens, G.; Fischer, H.; Gurk, C.; Klupfel, T.; et al. Hydroxyl radicals in the tropical troposphere over the Suriname rainforest: comparison of measurements with the box model MECCA. *Atmos. Chem. Phys.* **2010**, *10*, 9705−9728.
(32) Whalley, L. K.; Edwards, P. M.; Furneaux, K. L.; Goddard, A.; Ingham, T.; Evans, M. J.; Stone, D.; Hopkins, J. R.; Jones, C. E.; Karunaharan, A.; et al. Quantifying the magnitude of a missing hydroxyl radical source in a tropical rainforest. *Atmos. Chem. Phys.* **2011**, *11*, 7223−7233.
(33) Hui, A. O.; Fradet, M.; Okumura, M.; Sander, S. P. Temperature Dependence Study of the Kinetics and Product Yields of the HO_2 + $CH_3C(O)O_2$ Reaction by Direct Detection of OH and HO_2 Radicals Using 2f-IR Wavelength Modulation Spectroscopy. *J. Phys. Chem. A* **2019**, *123*, 3655−3671.
(34) Christensen, L. E.; Okumura, M.; Sander, S. P.; Salawitch, R. J.; Toon, G. C.; Sen, B.; Blavier, J.-F.; Jucks, K. W. Kinetics of HO_2 + HO_2 → H_2O_2 + O_2: Implications for Stratospheric H_2O_2. *Geophys. Res. Lett.* **2002**, *29*, 13-1−13-4.
(35) Christensen, L. E.; Okumura, M.; Hansen, J. C.; Sander, S. P.; Francisco, J. S. Experimental and Ab Initio Study of the HO_2CH_3OH Complex: Thermodynamics and Kinetics of Formation. *J. Phys. Chem. A* **2006**, *110*, 6948−6959.
(36) Tang, Y.; Tyndall, G. S.; Orlando, J. J. Spectroscopic and Kinetic Properties of HO_2 Radicals and the Enhancement of the HO_2 Self Reaction by CH_3OH and H_2O. *J. Phys. Chem. A* **2010**, *114*, 369−378.
(37) Andersson, B. Y.; Cox, R. A.; Jenkin, M. E. The Effect of Methanol on the Self Reaction of HO_2 Radicals. *Int. J. Chem. Kinet.* **1988**, *20*, 283−295.
(38) Grieman, F. J.; Noell, A. C.; Davis-Van Atta, C.; Okumura, M.; Sander, S. P. Determination of Equilibrium Constants for the Reaction between Acetone and HO_2 Using Infrared Kinetic Spectroscopy. *J. Phys. Chem. A* **2011**, *115*, 10527−10538.
(39) Nielsen, O. J.; Johnson, M. S.; Wallington, T. J.; Christensen, L. K.; Platz, J. UV absorption spectra of HO_2, CH_3O_2, $C_2H_5O_2$, and $CH_3C(O)CH_2O_2$ radicals and mechanism of the reactions of F and Cl atoms with $CH_3C(O)CH_3$. *Int. J. Chem. Kinet.* **2002**, *34*, 283−291.
(40) Smarte, M. D. Modeling and Fitting of ALS MPIMS Kinetics, v1.2.0; Caltech Data, 2019. https://data.caltech.edu/records/1248.
(41) Keller-Rudek, H.; Moortgat, G. K.; Sander, R.; Sörensen, R. The MPI-Mainz UV/VIS Spectral Atlas of Gaseous Molecules of Atmospheric Interest. *Earth Syst. Sci. Data* **2013**, *5*, 365−373.
(42) Burkholder, J. B.; Sander, S. P.; Abbatt, J.; Barker, J. R.; Cappa, C.; Crounse, J. D.; Dibble, T. S.; Huie, R. E.; Kolb, C. E.; Kurylo, M. J.; et al. "Chemical Kinetics and Photochemical Data for Use in Atmospheric Studies, Evaluation No. 19" JPL Publication 19-5, Jet Propulsion Laboratory, Pasadena, 2019. http://jpldataeval.jpl.nasa.gov.

https://doi.org/10.1021/acs.jpca.3c03660
J. Phys. Chem. A 2023, 127, 7772−7792

(43) Levenberg, K. A. A method for the solution of certain non-linear problems in least squares. *Q. Appl. Math.* **1944**, *2*, 164−168.
(44) Marquardt, D. An Algorithm for Least-Squares Estimation of Nonlinear Parameters. *J. Soc. Ind. Appl. Math.* **1963**, *11*, 431−441.
(45) Parrish, D. D.; Trainer, M.; Young, V.; Goldan, P. D.; Kuster, W. C.; Jobson, B. T.; Fehsenfeld, F. C.; Lonneman, W. A.; Zika, R. D.; Farmer, C. T.; et al. Internal consistency tests for evaluation of measurements of anthropogenic hydrocarbons in the troposphere. *J. Geophys. Res.* **1998**, *103*, 22339−22359.
(46) NIST Computational Chemistry Comparison and Benchmark Database, NIST Standard Reference Database Number 101, Release 22, Editor: Russell D. Johnson III, 2022. http://cccbdb.nist.gov/.
(47) Aloisio, S.; Francisco, J. S.; Friedl, R. R. Experimental evidence for the existence of the HO_2-H_2O complex. *J. Phys. Chem. A* **2000**, *104*, 6597−6601.
(48) Kanno, N.; Tonokura, K.; Koshi, M. Equilibrium constant of the HO_2-H_2O complex formation and kinetics of HO_2 + HO_2-H_2O: Implications for tropospheric chemistry. *J. Geophys. Res.* **2006**, *111*, D20312.
(49) Kanno, N.; Tonokura, K.; Tezaki, A.; Koshi, M. Water dependence of the HO_2 self-reaction: Kinetics of the HO_2-H_2O complex. *J. Phys. Chem. A* **2005**, *109*, 3153−3158.
(50) Aloisio, S.; Francisco, J. S. Existence of a hydroperoxy and water (HO2·H2O) radical complex. *J. Phys. Chem. A* **1998**, *102*, 1899−1902.
(51) Hamilton, E.; Naleway, C. Theoretical calculation of stront complex formation by the HO_2 radical: HO_2-H_2O and HO_2-NH_3. *J. Phys. Chem.* **1976**, *80*, 2037−2040.
(52) Lendvay, G. Ab Initio studies of complexes of HO2 radicals with NH3, H2O, and HF. *Z. Phys. Chem.* **2001**, *215*, 3.
(53) Hamilton, E. J., Jr.; Lii, R.-R. The Dependence on H_2O and on NH_3 of the Kinetics of the Self-Reaction of HO_2 in the Gas-Phase Formation of HO_2·H_2O and HO_2·NH_3 Complexes. *Int. J. Chem. Kinet.* **1977**, *9*, 875−885.
(54) Bloss, W. J.; Rowley, D. M.; Cox, R. A.; Jones, R. L. Rate Coefficient for the BrO + HO_2 Reaction at 298 K. *Phys. Chem. Chem. Phys.* **2002**, *4*, 3639−3647.
(55) Takacs, G. A.; Howard, C. J. Temperature dependence of the reaction HO_2 + HO_2 at low pressures. *J. Phys. Chem.* **1986**, *90*, 687−690.
(56) Thrush, B.; Tyndall, G. The rate of reaction between HO_2 radicals at low pressure. *Chem. Phys. Lett.* **1982**, *92*, 232−235.
(57) Kircher, C. C.; Sander, S. P. Kinetics and mechanism of HO_2 and DO_2 disproportionation. *J. Phys. Chem.* **1984**, *88*, 2082−2091.

https://doi.org/10.1021/acs.jpca.3c03660
J. Phys. Chem. A 2023, 127, 7772−7792